MARTA AGNIESZKA BRZEZIŃSKA

BEYOND THE TEN-FOLD WAY: NOVEL TOPOLOGICAL PHASES IN LOW-DIMENSIONAL SYSTEMS

BEYOND THE TEN-FOLD WAY: NOVEL TOPOLOGICAL PHASES IN LOW-DIMENSIONAL SYSTEMS

A dissertation submitted to attain the degree of

DOCTOR OF SCIENCES of WROCŁAW UNIVERSITY OF SCIENCE AND TECHNOLOGY

presented by

MARTA AGNIESZKA BRZEZIŃSKA

Master of Science in Physics,

Wrocław University of Science and Technology, Poland

born on 22 August 1991

supervised by

Prof. Titus Neupert,

Prof. Arkadiusz Wójs,

Dr. Paweł Potasz

2020

ABSTRACT

This thesis covers selected recent developments in the field of topological aspects of condensed matter physics. In particular, we focus on three directions which can be seen as extensions of well-established classification of free-fermionic gapped states: i) investigating a realization of topological states in the systems defined in non-integer spatial dimensions, ii) the role of crystal symmetries and how they affect the distinction between topologically trivial and non-trivial states, and iii) non-Hermitian Hamiltonians arising from a minimal modelling of gains and losses exhibiting observable phenomena without Hermitian counterparts. In all cases, we propose material candidates or experimental setups to support our theoretical findings.

ABSTRAKT

Przedłożona rozprawa doktorska obejmuje wybrane najnowsze osiągnięcia w dziedzinie topologicznych aspektów fizyki materii skondensowanej. W szczególności uwaga zostanie poświęcona trzem kierunkom badań, które można postrzegać jako rozszerzenie ugruntowanej klasyfikacji układów nieoddziałujących fermionów: i) próba realizacji stanów topologicznych w układach scharakteryzowanych przez liczbę wymiarów przestrzennych będących liczbą niecałkowitą, ii) rola symetrii krystalicznych i ich wpływ na rozróżnienie pomiędzy stanami topologicznymi oraz trywialnymi, a także iii) hamiltonianami niehermitowskimi będącymi efektywnym opisem układów otwartych i wykazującymi obserwowalne zjawiska bez odpowiedników w modelach hermitowskich. We wszystkich omawianych zagadnieniach zostaje przedyskutowana możliwa realizacja eksperymentalna w celu poparcia wyników teoretycznych.

ACKNOWLEDGEMENTS

First of all, I would like to thank my supervisors from Wrocław University of Science and Technology, for helping me during the first years of my PhD studies and encouraging me to work in the field of condensed matter physics.

I would like to thank Titus Neupert for giving me the life-changing opportunity to pursue my research in Switzerland and my colleagues from Condensed Matter Theory Group at University of Zurich - I had a great time with having you around.

I also want to thank my family for their constant support and love.

CONTENTS

LIST OF TABLES

1D, 2D, ...	one-dimensional, two-dimensional, ...
AZ	Atland-Zirnbauer
BZ	Brillouin zone
CB	conduction band
CHS	chiral symmetry
DFT	density functional theory
DOS	density of states
EE	entanglement entropy
ES	entanglement spectrum
IR	irreducible representation
NN	nearest-neighbour
NNN	next-to-neares nearest-neighbour
PHS	particle-hole symmetry
QHE	quantum Hall effect
SG	space group
SLS	sublattice symmetry
SOC	spin-orbit coupling
SPT phase	symmetry-protected topological phase
TI	topological insulator
TRIM	time-reversal invariant momentum
TRS	time-reversal symmetry
VB	valence band

INTRODUCTION

Classification is a theme that lies at the heart of condensed matter physics. For a long time, it was believed that Ginzburg-Landau theory [1] of the phase transitions based on the symmetry-breaking paradigm provides a complete list of phases of matter. It states that the continuous transition between phases is described by a local order parameter, which vanishes in the high-symmetry (disordered) phase and becomes non-zero in the low-symmetry (ordered) phase. For instance, magnetization serves as an order parameter at the ferromagnetic-paramagnetic transition; crystals break continuous translational symmetry and hence are characterized by a discrete space group. Another example is superconductivity, where the non-zero gap Δ indicates the superconducting state.

At the beginning of 1970s, Berezinskii [2, 3], Kosterlitz and Thouless [4, 5] investigated a two-dimensional classical magnet with $U(1)$ (XY model) in which the phase transition falls beyond the Ginzburg-Landau paradigm. At the zero-temperature, the system is ferromagnetic as the spins are perfectly arranged. At finite (but small) temperature, the system still has long-range correlations but a local spin structures called vortices may be created. Vortices are said to be topological excitations as the only way to destroy them is to annhilate vortex with an antivortex. With an increase of the temperature, more pairs of vortex-antivortex pairs are created and they become less bounded, hence destroying the long-range correlations. This is the Kosterlitz-Thouless (KT) phase transition in which no continuous symmetry is spontaneously broken (which is in an agreement with Mermin-Wagner theorem), yet the system undergoes a transition to the phase with short-range correlations. For their developments in the field of topological matter, Kosterlitz and Thouless (together with Haldane) obtained the Nobel Prize in 2016.

An even more pronounced example is a discovery of the integer quantum Hall effect (IQHE) [6], and subsequently, the fractional version of this phenomenon (FQHE) [7]. In a two-dimensional electron gas at low temperature exposed to a strong magnetic field, applying the voltage on the two sides of a sample results in a current generated in the perpendicular direction. As a function of the magnetic field, one observes the perfectly flat plateaus in the transverse Hall conductivity, while the longitudinal conductivity vanishes. Hall conductivity σ_{xy} takes quantized values being multiplies ν (ν is an integer in case of IQHE, while a fraction in case of FQHE) of elementary constants e^2/h (where e is the electron charge and h is the Planck constant) and has been measured to the accuracy of the order 10^{-9} [8]. For the discovery of IQHE, Klaus von Klitzing got the Nobel Prize in 1985 and now the quantum of conductance serves as a universal constant. The origin of this quantization is universal, in a sense that it is observed regardless of microscopic details of a sample such as disorder. In a finite geometry, the systems exhibits robust edge currents, which are chiral, that is they flow in one fixed direction. These are two different manifestations of the topological properties of the systems.

IQH states can be understood from the perspective of the Landau levels formed in a strong magnetic field. A remarkable idea given by Thouless, Kohmoto, Nightingale, and den Nijs (TKNN) [9] was to relate the number of gapless edge modes with the topological invariant computed for the bulk. This became the first observation of the *bulk-boundary correspondence*. Later on, the theoretical proposals of realization of IQH states on the honeycomb lattice in the absence of magnetic field [10] or topological superconductors [11] ignited the experimental search for topological materials. On the other hand, understanding FQHE requires

taking into account the electron-electron interactions. The exotic properties emerge from the collective behavior of electrons and give rise to the concept of topological order as the low-energy effective theory can be described in terms of topological quantum field theories (such as Chern-Simons or BF). Apart from FQHE, another paradigmatic example of topological order is chiral spin liquid developed as an attempt to understand high-temperature superconductivity [12, 13]. Topologically ordered states may posses unique features such as fractionalized excitations (carrying the fractions of elemental charge) with the anyonic exchange statistic (not bosonic nor fermionic) or long-range entanglement pattern [14]. In addition, they exhibit robust ground state degeneracy depending on the manifold on which they are defined. These properties are very promising for a fault-tolerant quantum computing [15].

As no symmetry breaking occurs, in order to classify topological phases a notion of equivalence classes has to be introduced. To do so, we will investigate the systems at zero temperature with a spectral gap separating the ground state from the first excited state. States are said to be topologically equivalent if they can be connected by unitary transformations that act infinitely slowly (adiabatically). The physical constrains of unitaries are that at every point of evolution they have to preserve the energy gap and they have to involve only local degrees of freedom. In addition, one may take into account the symmetries to enlarge the number of possible unitary transformations and investigate symmetry-protected (or symmetry-enriched) topological states.

Not all the states that are topological posses intrinsic topological order: some of them may be short-range entangled and they can be understood from the single-particle physics perspective (a more detailed explanation will be given in the following chapter). Interestingly, a lot of theoretical developments were followed-up by experimental efforts.

ORGANIZATION OF THIS THESIS

In this thesis, we study non-interacting fermionic systems which cannot be completely classified by means of the so-called ten-fold way, that is the classification based on a dimensionality and the presence or absence of internal symmetries: time-reversal, particle-hole and chiral.

Chapter 1 serves as a brief introduction to topological band theory, with an emphasis on the basic definitions, topological invariants and illustrative examples of toy models.

In Chapter 2, a realization of topological states in systems with non-integer spatial dimension is discussed. Detecting topological properties without the translational invariants requires employing real-space methods

Chapter 3 is devoted to the states protected by the crystalline symmetries. However, they fall beyond a sharp distinction what is topological or trivial. Obstructed atomic limits are recent refinements and can be understood from the perspective of Wannier functions.

Topological states in non-Hermitian systems are investigated in Chapter 4. Recently, a studies of non-Hermitian Hamiltonians emerged as an effective modeling of open systems in which the energy or particle number is not preserved.

Finally, Chapter 4.3.1 provides a summary and indicates further directions.

In addition, some lengthly derivations are given in Appendix **??**.

1

TOPOLOGICAL BAND THEORY

In this chapter, we introduce more formally the concept of topology in the band theory. We provide the definitions of topological invariants, precise the bulk-boundary correspondence, and discuss the details of the classification for gapped free-fermion models.

1.1 NOTION OF TOPOLOGY

Topology is a branch of mathematics that deals with properties of smooth, continuous transformations. It ignores the geometrical details of an object, but rather focuses on global features that can be described by topological invariants We briefly introduce fundamental concepts [**Nakahara**].

Figure 1.1: From a perspective of topology, the

1.1.1 *Homotopy and equivalence classes*

Consider two smooth manifolds X, Y. Then continuous maps $f_0 : X \to Y$ and $f_0 : XY$ are homotopically equivalent if there is a continuous maps

$$F : [0,1] \times X \to Y \tag{1.1}$$

$F(0,x) = f_0(x)$ and $F(1,x) = f_1(x)$ for all $x \in X$.

Hence, in order to change

1.2 SYMMETRIES AND CLASSIFICATION OF TOPOLOGICAL INSULATORS AND SUPERCONDUCTORS

In quantum mechanics, the symmetries are constructed according to the Wigner's theorem: they are the operators that preserve transition probabilities and are therefore implemented via unitaries or antiunitaries which commute with the Hamiltonian.

A local unitary symmetry can be decomposed as $U = U_1 \dots U_n$, where each U_i affects only a small region in space. Conversely, a non-local unitary

A fundamental example of antiunitary operator is the time-reversal, which takes $t \to -t$. Acting on Hamiltonian H:

$$\mathcal{T} H \mathcal{T}^{-1} = +H \tag{1.2}$$

As all antiunitary operators, $\mathcal{T}$ can be decomposed into a product of a unitary operator T and complex conjugate $\mathcal{K}$, $\mathcal{T} = T\mathcal{K}$. Applying $\mathcal{T}$ twice will lead to the rise of the phase factor, hence $\mathcal{T}^2 = \pm 1$. This is true for all antiunitary symmetries. For spin-1/2 systems,

5	6	$\mathcal{T}$ 7	$\mathcal{P}$ 8	$\mathcal{C}$	1	2	3	4
standard -	A (unitary) $\mathbb{Z}$	0 - $\mathbb{Z}$	0	0	-	$\mathbb{Z}$	-	$\mathbb{Z}$
	AI (orthogonal)	+1	0	0	-	-	-	
	AII (symplectic)	-1	0	0	-	$\mathbb{Z}_2$	$\mathbb{Z}_2$	
chiral $\mathbb{Z}$	AIII (chiral unitary) -	0 $\mathbb{Z}$	0 -	1	$\mathbb{Z}$	-	$\mathbb{Z}$	-
	BDI (chiral orthogonal)	+1	+1	1	$\mathbb{Z}$	-	-	
	CII (chiral symplectic)	-1	-1	1	$\mathbb{Z}$	-	$\mathbb{Z}_2$	
BdG	D	0	+1	0	$\mathbb{Z}_2$	$\mathbb{Z}$	-	
	C	0	-1	0	-	$\mathbb{Z}$	-	
	DIII	-1	+1	1	$\mathbb{Z}_2$	$\mathbb{Z}_2$	$\mathbb{Z}$	
	CI	+1	-1	1	-	-	$\mathbb{Z}$	

Table 1.1: Table of symmetry classes of non-interacting Hamiltonians. 0 corresponds to the absence of symmetry and $\pm$ 1 indicates the sign to which the symmetry squares

TRS systems follow the Kramers' theorem which tells that all states comes in time-reversal symmetric pairs $\mathcal{T}|n\rangle = |n\rangle$.

Another (antiunitary) symmetry is the particle-hole $\mathcal{P}$, defined as:

$$\mathcal{P}H\mathcal{P}^{-1} = -H \tag{1.3}$$

Finally, we can define chiral symmetry being a product of $\mathcal{T}$ and $\mathcal{P}$, $\mathcal{C} = \mathcal{T}\mathcal{P}$ [1]

$$\mathcal{C}H\mathcal{C}^{-1} = -H \tag{1.4}$$

$\mathcal{C}$ may be present in the system, even if $\mathcal{T}$ and $\mathcal{P}$ are absent. Although chiral symmetry in not a symmetry in a strict sense, but guarantees that non-zero eigenvalues of the Hamiltonian come in pairs, hence there is a spectral symmetry.

Dates back to the idea of Élie Cartan's classification of symmetric spaces in differential geometry. Later on, Altland and Zirnbauer applied this classification in the context of random matrix theory [16]

All possible combination of internal symmetries in $d = 1, \ldots, 8$ spatial dimensions are tabulated in Tab. 1.2. There are ten distinguished classes.

This was first proposed in Ref. [17], with further mathematical improvements from K-theory (such is pattern called Bott periodicity; with a period two for the complex classes AI, AIII and a period eight for remaining eight real classes) given by Kitavev [18] to finally provide the complete classification [19].

For higher dimensions, topological invariants repeat themselves and show the Bott periodicity with period 2 for classes A and AIII, and period 8 for the remaining ones.

1 Note that $\mathcal{P}$ and $\mathcal{C}$ anticommute with the single-particle Hamiltonian

1.3 TOPOLOGICAL INVARIANTS

1.3.1 *Geometrical phases and adiabatic evolution*

Berry connection of Bloch states:

$$\mathbf{A} = i \langle u_n(\mathbf{k}) | \Delta | u_m(\mathbf{k}) \rangle \tag{1.5}$$

$\Delta \equiv \Delta_{\mathbf{k}}$ Berry curvature:

$$F = \Delta \times \mathbf{A} \tag{1.6}$$

Gauss-Bonnet theorem for a two-dimensional manifold M without a boundary:

$$\int_M K dA = 2\pi(2 - 2g) \tag{1.7}$$

with K being the Gauss curvature and g - genus.

1.3.2 *Chern number*

For two-dimensions, it is given by the (first) Chern number:

$$C = \frac{1}{2\pi} \int_{BZ} F \tag{1.8}$$

(note, some conventions incorporate imaginary unit i explicitly in the prefactor).

1.3.3 *Z_2 topological index*

Some systems can have one trivial and one topological phase, which is characterized by a two-valued index ν being 0 or 1, respectively. Z_2 invariant can be computed easily in the presence of inversion symmetry using Fu-Kane formula [20]:

$$\delta_i = \prod_{m=1}^{N} \xi_{2m}(\Gamma_i); \qquad (-1)^{\nu} = \prod_i \delta_i \tag{1.9}$$

where Γ_i are time-reversal invariant momenta in the BZ, $\xi_{2m}(\Gamma_i)$ is every second occupied Kramers pair. In case of 3D systems, two types of TI can be observed, defined whether they have a strong or weak indices. Non-zero strong index means that the system cannot be seen as a set of stacked 2D layers, it's intrinsically three-dimensional.

Because for TRS systems C always vanishes, if S_z (spin component pointing out of 2D plane) is conserved, one may define the spin Chern number [21] based on the fact that spins up and down have independent Chern numbers:

$$C_s = \frac{C_\uparrow - C_\downarrow}{2} \tag{1.10}$$

and is related to ν as $\nu = C_s \mod 2$

Pffafian formalism

1.4 TOPICAL EXAMPLES

In the following, we would like to discuss relevant examples of toy models and discuss experimental realizations.

1.4.1 *Class BDI: Su-Schriffer-Heeger chain*

SSH model, firstly proposed to describe polyacetylene, describes spinless fermions in 1D chain [22]

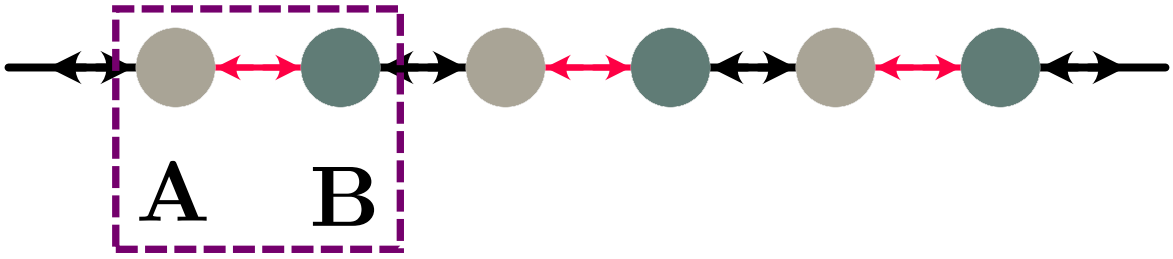

Figure 1.2: A schematic of SSH chain. There are two atomic sites A and B per unit cell and alternating hoppings with strength t (within unit cell) and t' (between neighbouring unit cells). Depending on t and t', the model exhibits two phases: if $t' > t$, the system is in a topological phase with gapless edge modes in an open geometry; conversely, if $t' < t$ the system is in a trivial phase with $t' = 0$ as a fully dimerized case.

Bloch Hamiltonian reads:

$$H(k) = \begin{pmatrix} 0 & t + t'e^{ik} \\ t + t'e^{-ik} & 0 \end{pmatrix} \tag{1.11}$$

Dispersion

$$E(k) = \pm\sqrt{t^2 + t'^2 + 2tt'\cos k} \tag{1.12}$$

The system has the chiral symmetry realized by σ_z, particle-hole $P = \sigma_z\mathcal{K}$ and time-reversal $\mathcal{T} = \mathcal{K}$. Here, It is the chiral symmetry that protects the topological properties and, for instance, adding long range hoppings would destroy topological states.

1.4.2 *Class A*

1.4.2.1 *Quantum Hall effect*

IQH states can be seen as the most robust topological states without intrinsic topological order as they don't need any symmetry to persist. In particular, TR is broken. Actually, in the classification based on the entanglement (Wen vs. Kitaev),

Let us start from a semiclassical description of the QH effect. In the bulk, electrons do not move freely through the sample, but rather follow circular trajectories with a radius $l_B = \sqrt{\hbar/eB}$. However, at the edges the orbits do not form closed loops and contribute to the current flow. Edge current will not disappear in presence of disorder and is not affected by the detailed shape of a sample. Recall the

A consequence of non-trivial bulk topology is the presence of gapless edge modes at the interface between systems with different topologies (for instance, trivial vacuum). They are chiral, that is, they propagate along the edge only in one direction.

1.4.2.2 *Chern insulators*

Haldane model is a canonical example of a Chern insulator. It describes spinless electrons in a single honeycomb lattice, where staggered potential M breaks inversion symmetry and the complex next-nearest-neighbour hoppings breaking TR symmetry arise due to to

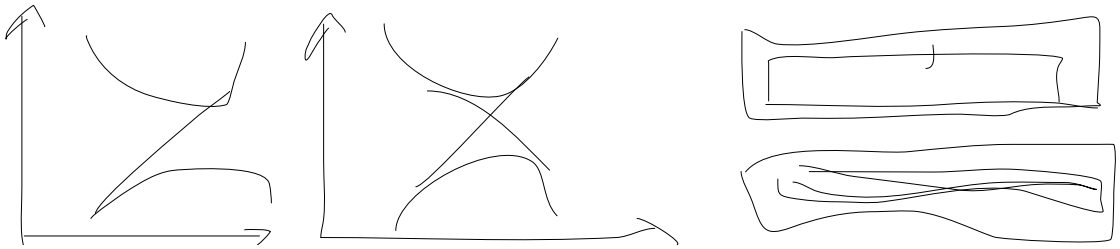

Figure 1.3: Left: Schematic representation of the band structures of (a) Chern insulator with $C = +1$ and (b) QSH system constructed as two copies of CI with opposite Chern numbers, together with conserved z-spin component. Right: Edge modes flowing in samples

Aharanov-Bohm phases. It is possible to choose the AB phases such that net magnetic field in an unit cell is zero (in contrast to the quantum Hall effect).

Peierls substitution:

$$r_{xy} \to t_{xy} \exp\left(-\mathrm{i}\frac{e}{h}\int_{\Gamma} \mathbf{A}\cdot d\ell\right) \tag{1.13}$$

Staggered mass term M is defined

$$H_{Haldane} = -t\sum_{\langle i,j\rangle}\hat{c}_i^\dagger\hat{c}_j - t'\sum_{\langle\langle i,j\rangle\rangle} e^{\mathrm{i}\varphi}\hat{c}_i^\dagger\hat{c}_j + \sum_i M_i\hat{c}_i^\dagger\hat{c}_j + h.c., \tag{1.14}$$

where $\langle\ldots\rangle$ corresponds to real-valued hoppings between nearest neighbours, and $\langle\langle\ldots\rangle$ to the next-nearest neighbours

Experimental realizations include fermionic ultracold atoms [23] or classical wave systems [24].

1.4.3 *Class AII: quantum spin Hall effect*

In 2005, Kane and Mele extended the notion of Chern insulators by taking two copies of Haldane model with opposite chiralities [25]. This lead to the construction of a insulating state which is time-reversal invariant and has protected gapless edge modes lying in the bulk gap, where the topological properties are defined by a $\mathbf{Z}_2$ invariant. Edge states are helical - that is, they two states counterpropagate along a boundary They also come in time-reversal pairs according to the Kramers' theorem. States with odd number of Kramers' edge pairs are topological, while with even number - are topologically trivial. Another consequence of the TR symmetry is that energy levels crossing appear only at special points in the BZ. Authors suggested that this model may be realized in graphene, however due to negligible spin-orbit coupling, it is not realizable experimentally under realistic conditions [26, 27]. Besides fundamental theoretical interest, QSH states hold great promise for spintronics as it is possible to manipulate spin degrees of freedom in the absence of magnetic field [28].

Subsequently, QSH effect was proposed in strained zinc-blende semiconductors (such as gallium arsenide) [29]. Bernevig, Hughes and Zhang [30] predicted a quantum phase transition in HgTe/CdTe quantum wells as a function of the thickness. This happens because of a band inversion due to strong spin-orbit coupling in HgTe: CB has a p-like character and VB is composed of s-orbitals instead of normal ordering which is observed in CdTe: s-orbital character of conduction band and p-orbital of valence band. It was confirmed experimentally year later by observing quantized resistance $h^2/2e$ (factor 2 comes from the spin contribution) [31]. This ignited a search for new materials exhibiting QSH states [32, 33], and topological insulators in three-dimensions.

In Ref. [34]

2

TOPOLOGICAL STATES IN FRACTAL LATTICES

In the previous chapter, we have shown the importance of internal symmetries and dimensionality in building a classification of different free-fermionic Hamiltonians. Most of the topological phases in distinct symmetry classes are studied by considering clean systems limit, where it is possible to employ the concepts related to the Brillouin zone. However, disordered systems or lattice models without translational symmetries may also host topological states. For instance, quasicrystals, aperiodic systems that posses long-range order [35], exhibit topological properties which arise from higher-dimensional space in which these structures are truly translational invariant [36]. Several tilings were used to construct quasicrystalline structures hosting topological states protected by the symmetries which are forbidden for conventional crystals, including five- or twelve-fold rotations [37, 38]. Moreover, topological phases can be realized in completely random point sets [39]. Another interesting example is the so-called statistical topological insulator, where the gapless surface states are immune to Anderson localization as long as the disorder ensemble is invariant under a certain symmetry [40].

Self-similar lattices, in particular fractals [41], also fall into the category of aperiodic systems. Rather than a translational invariance, they posses a scale invariance and are characterized by a Hausdorff dimension d_{H}, which is not necessary an integer. A concept of fractals has been extensively studied in the context of condensed matter physics, ranging from spin models defined on fractal lattices [42, 43] to the multifractal structure of wave functions at the Anderson metal-insulator transition point [44]. More recent studies covered quantum transport [45] and optoelectronic properties [46, 47] in fractal geometries, localization in deterministic and random fractal lattices [48–50], or defects in regular lattices arranged in a fractal manner [51]. Progress in the field in not only restricted to theoretical predictions – artificial fractal structures have been already experimentally realized using focused ion beam epitaxy [52], by depositing atoms on a surface [53] or assembling molecules [54].

Since it is possible to define quantum states on general graphs, it is important to ask what type of properties a graph must have to host topological states (notably, to define the topology of quantum states, only a notion of locality and the possibility to take a thermodynamic limit are required). Here, we would like to address this question by examining two fractal lattice, Sierpiński carpet (SC) and Sierpiński gasket (or triangle, SG), in a homogeneous magnetic field. Sierpiński carpet and gasket are different in terms of their dimensionality and connectivity properties. Recall, the Hausdorff dimension is given as

$$d_{\mathrm{H}} = \frac{\ln A}{\ln L} \tag{2.1}$$

where A is the covered area of a fractal with linear extend L. For SC, $d_H \approx 1.892\ldots$, while for SG $d_H \approx 1.585$. Another property, ramification number $\mathcal{R}$, is said to be finite if after eliminating a finite number of bonds one can isolate an arbitrarily large part of a system. For SC, $\mathcal{R} = \infty$, while SG has finite ramification $\mathcal{R} = 4$.

Even though spectral properties of SC and SG were investigated before [55–58], topological aspects of the Hamiltonians defined on such lattices remain not fully explored. Authors in Ref. [59] reported results on BHZ model defined on three distinct fractal geometries, while

in Ref. [60] construction of spinless chiral $p-$ and $p+ip-$wave superconductors on SC and SG was discussed. Understanding the bulk-boundary correspondence in such systems is problematic as well as there is no sharp distinction between the bulk and edge. It was found that the edge states in SC corresponding to non-zero σ_{xy} are always present for a finite field strength and stable as one approaches the thermodynamic limit [61]. On the other hand, the Hall conductivity is not always proportional to the Chern number [62]

As a final motivation to investigating Hamiltonians on fractals is related to the fractons. Fractonic topologically ordered models host fractionalized point-like excitations, fractons, which are immobile. In some of them (called type-II) operators that create excitations have support on a fractal subset of the three-dimensional lattice.

2.1 MODEL

We investigate the lattice regularization of two aforementioned geometries (consult Fig. 2.1). Complex fractal pattern can be generated by the iterative procedure in which the system size increases with every step, but the distance between lattice sites remains the same. Such setting is most relevant to potential experiments on a nanoscopic scale as it introduces a natural cutoff. In order to construct the carpet, we start with a simple square lattice with $L(n) = 3^n$ sites along the outer edge, where n is an iteration step. Then, in every step n, $(1-(8/9)^n)\cdot 9^n$ lattice sites are removed. From the Pascal's triangle modulo m (with m being a prime number) embedded in a triangular lattice having 2^n+1 rows, it is possible to obtain a series of gasket-like lattices with $d_H = 1+\log_m\left(\frac{m+1}{2}\right)$ and the case of $m=2$ corresponds to SG.

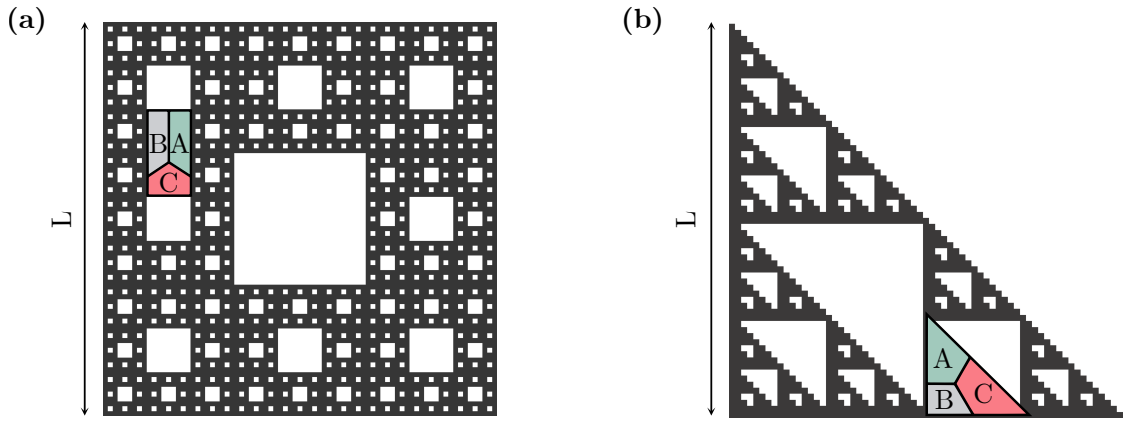

Figure 2.1: Fractal lattices: (a) the forth iteration of the Sierpiński carpet with $L = 81$ and **(b)** the sixth iteration of the Sierpiński gasket with $L = 65$. Black squares depict the lattice sites which are kept from underlying regular square (in case of carpet) and triangular (gasket) lattices. Summation regions used in real-space Chern number calculations are labeled with A, B, C.

In the following, we consider a tight-binding Hamiltonian describing non-interacting spinless fermions exposed to a perpendicular magnetic field

$$H = -t\sum_{\langle i,j\rangle} e^{\mathrm{i}A_{ij}} c_i^\dagger c_j + \text{h.c.}, \tag{2.2}$$

where i labels lattice sites. The hopping integral t between nearest-neighbors is the only energy scale in the model and it is set to $t=1$. Magnetic field is taken into account by employing Peierls substitution which gives rise to the phase factors $A_{ij} = \int_i^j \mathbf{A}\cdot d\mathbf{r}$, with $\mathbf{A}$

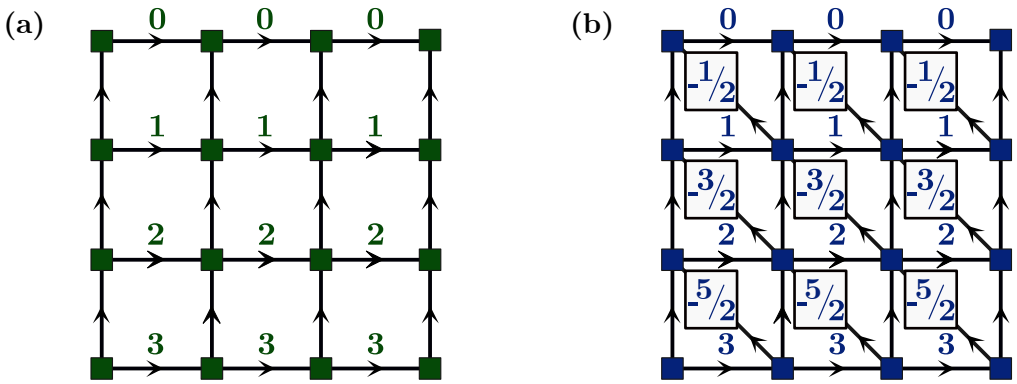

Figure 2.2: Vector potential gauge choice: Phase distribution on 4×4 **(a)** square and **(b)** triangle lattices with open boundary conditions. A_{ij} phase between sites i and j is equal to the number shown above the bond in 2π units. A phase acquired with the respect to the direction pointed by arrows has a positive sign.

being the vector potential satisfying relation $\mathbf{B} = \nabla \times \mathbf{A}$. We assume that the magnetic field is homogeneous in the two-dimensional space in which the fractal lattice is embedded. The magnetic flux per smallest element of lattice-regulated versions of carpet and gasket (that is, the smallest square in the SC and the smallest triangle for the SG) is chosen to be Φ, a fraction α of the flux quantum Φ_0. In units where $\hbar = e = 1$, $\Phi_0 = 2\pi$, hence $\Phi/\Phi_0 = \alpha$. The phase factors distribution is presented in Fig. 2.2.

2.2 SPECTRAL PROPERTIES

Firstly, let us focus on the energy spectra obtained by diagonalizing the Hamiltonian given in Eq. (2.2) for different values of the magnetic flux. In Fig. 2.3 (a, d), we show the density of states (DOS) for the SC at iteration $n = 4$ and the SG at iteration $n = 6$ with open boundary conditions. Discrete sets of energy levels E_λ are smoothed using a Gaussian function $f(E,\alpha) = \sum_\lambda \exp\left\{-\left[E - E_\lambda(\alpha)\right]^2/\eta\right\}$ with broadening $\eta = 0.001$. As in case of regular lattices, a presence of magnetic field gives rise to the self-similar spectrum in the energy-flux plane known as Hofstadter's butterfly [63]. The spectrum of the SC (see Fig. 2.3 (a)) is reflection-symmetric with respect to the $E = 0$ and the $\alpha = 1/2$ lines due to a chiral symmetry of the Hamiltonian on this bipartite lattice. Two finite gaps of maximal extend in energy ~ 0.1 are observed for small range of the flux around $\alpha = 1/4$, $3/4$ and $E = 0$. Regions of low DOS (which are fully gapped if periodic boundary conditions are assumed) host states with distinct localization properties, which are discussed in more details in Section 2.3. Fig. 2.3 (d) shows the spectrum of the SG, which has only a point-inversion symmetry about $\alpha = 1/2$ and $E = 0$, and exhibits various fully gapped regions. Large DOS appears around two points: $\alpha = 1/4$, $E \approx 1.4$ and symmetry-related $\alpha = 3/4$, $E \approx -1.4$. It is known that at zero flux the spectrum is fractal and the energy levels are macroscopically degenerated [64]; introducing a finite field leads to lifting this degeneracy.

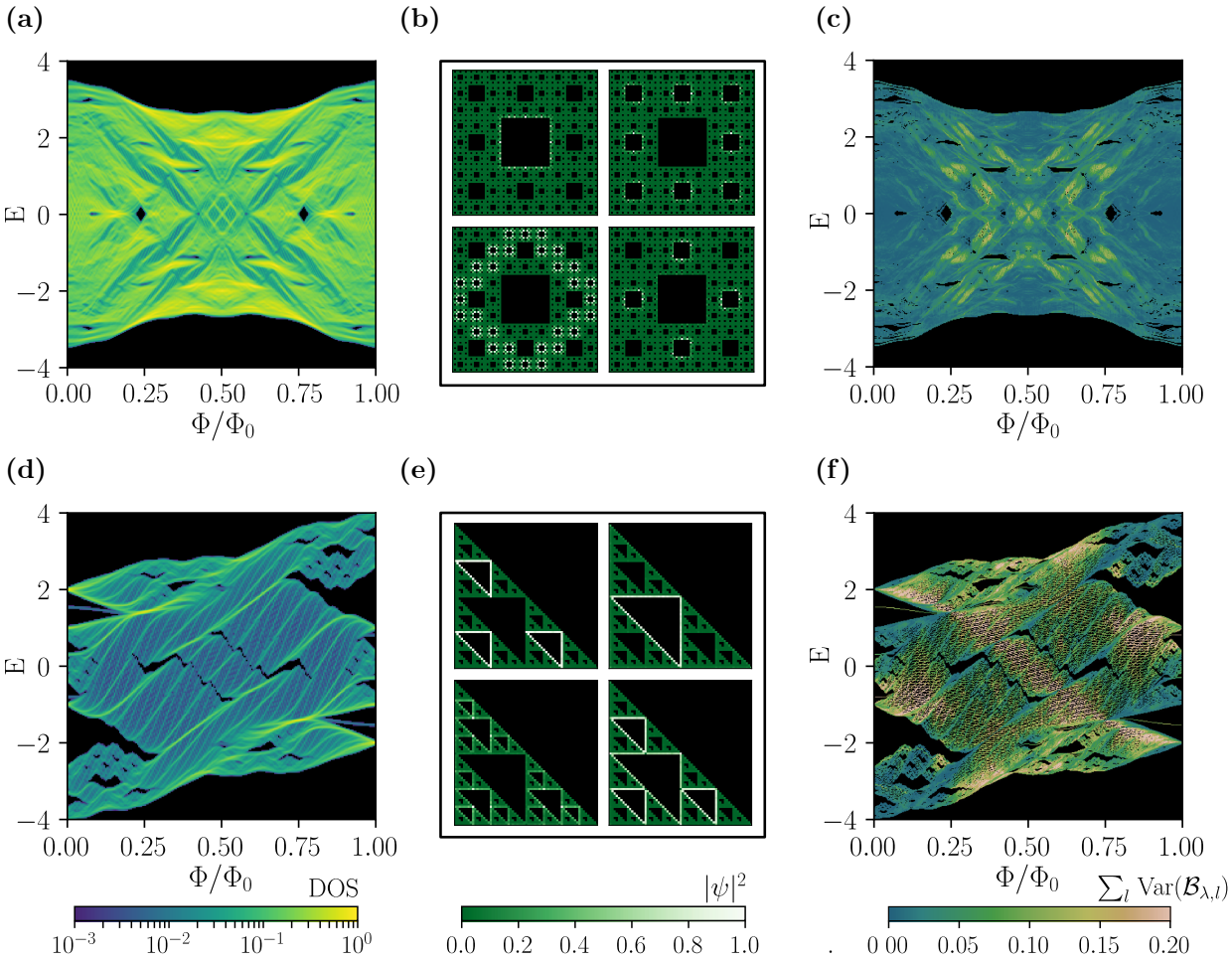

Figure 2.3: Spectral and eigenstate localization properties: (a, d) Density of states in the energy-flux plane, **(b, e)** localization of the eigenstates, and **(c, f)** edge-locality marker. Low DOS regions are represented by dark blue color. Two energy gaps at $E = 0$ are seen for SC, while the energy spectrum of SG exhibits numerous gaps. Representative electronic densities at time-reversal symmetric point ($\alpha = 1/2$) around $E = 0$ are presented in **(b, e)** and the color scale corresponds to the square modulus $|\psi_i|^2$ of the wave function normalized by its maximum value. $\mathcal{B}_{\lambda,l}$ marker shown in **(c, f)** quantifies the changes in localization properties between consecutive eigenstates at fixed flux. Parts of the spectra with smaller density are associated with largely varying values of edge-locality marker.

2.3 EDGE MODES

A striking feature of a conventional integer quantum Hall setup is the existence of protected edge modes. As a distinction between bulk and boundaries in fractal lattices is not sharp, it is crucial to investigate the localization eigenstate properties more carefully. Previous studies of fractal lattices suggested [65, 66] that introducing a magnetic field leads (on average) to delocalization of eigenstates. This observation can be confirmed by computing inverse participation ratio (IPR)

$$I_\psi = \frac{\sum_i |\psi_i|^4}{\left(\sum_i |\psi_i|^2\right)^2}, \tag{2.3}$$

for any wavefunction expandable in a site basis $|\psi\rangle = \sum_i \psi_i |i\rangle$. IPR takes values between 1 and the inverse of the number of sites N, where 1 corresponds to perfect localization at

one site and $1/N$ to evenly distributed weights over all lattice sites. At zero flux $\alpha = 0$, the distribution of IPRs is peaked close to the inverse of the number of sites belonging to the edges of the second-smallest squares or triangles. For a finite field, the distribution of IPRs shifts to smaller, i.e., more delocalized values. This effect is more apparent for the SC compared to the SG.

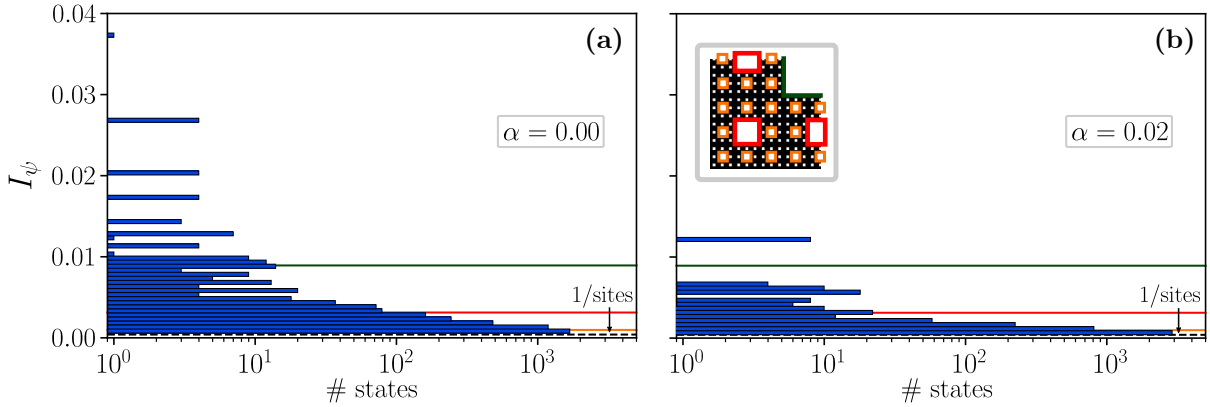

Figure 2.4: Distribution of IPR for Sierpiński carpet: at **(a)** $\alpha = 0$ and **(b)** $\alpha = 0.02$. Inset presents a closeup of carpet with internal edges of different hierarchies marked with different colors.

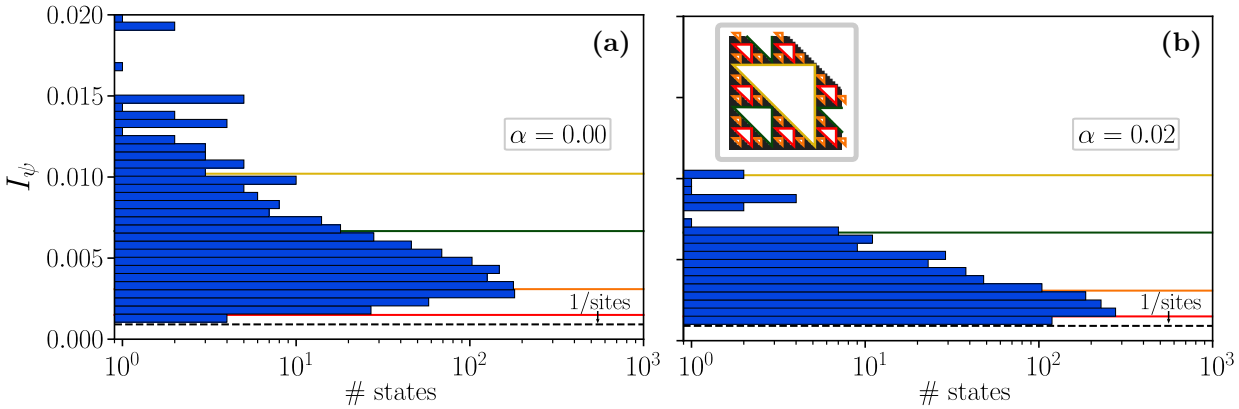

Figure 2.5: Distribution of IPR for Sierpiński gasket: at **(a)** $\alpha = 0$ and **(b)** $\alpha = 0.02$. Inset displays a closeup of gasket with highlighted edges of different hierarchies.

Remarkably, by contrasting the case of zero and non-zero magnetic field, we observe an intriguing change in the character of the most localized states. Fig. 2.3 (b, e) show the electronic densities for the eigenstates at the time-reversal symmetric point ($\alpha = 1/2$) around zero energy. States are sharply localized at the internal edges of the fractal at different levels of the hierarchy and they can be found in very close spectral proximity to one another in various places of the phase diagram at finite magnetic field. Conversely, at zero magnetic field, the most localized states are usually not supported on internal edges. To quantify the degree of localization, we compute edge-locality marker defined as

$$\mathcal{B}_{\lambda,l} = \sum_{i \in \mathcal{E}_l} |\psi_{\lambda,i}|^2, \tag{2.4}$$

where $\langle i|\psi_\lambda\rangle = \psi_{\lambda,i}$ and the summation is taken over the edges $\mathcal{E}_l$ of all internal triangles or squares at level l of the hierarchy. Hence, $\mathcal{B}_{\lambda,l}$ measures how much an eigenstate $|\psi_\lambda\rangle$ with an energy E_λ has a support on different edges of hierarchy level l. With every state $|\psi_\lambda\rangle$,

we associate a set of $\mathcal{B}_{\lambda,l}$ for $l = 0, \ldots, n$. In order to detect where in the phase diagram the localization properties are varying at most, we compute the variance for each entry of the set $\mathcal{B}_{\lambda,l}$ across three states with energies $E_{\lambda-1}$, E_λ and $E_{\lambda+1}$, and sum these variances over l. Results shown in Fig. 2.3 (c, f) indicate that sharp changes in eigenstate localization appear mostly in the low DOS regions, thus we can interpret these regions as made of edge-like states at various levels of the fractal hierarchy.

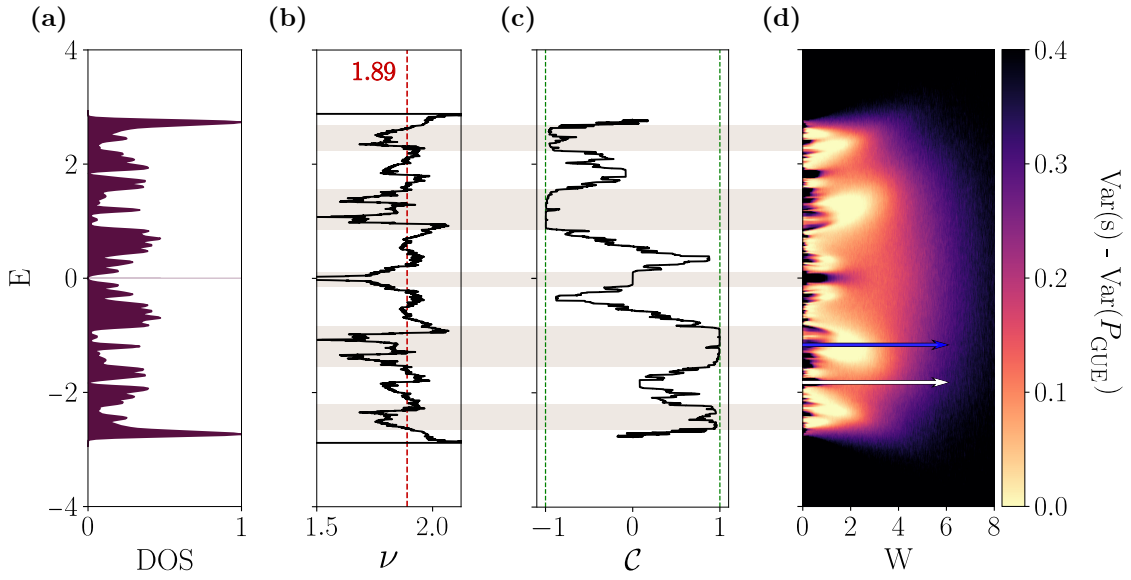

Figure 2.6: Detecting topological properties of Sierpiński carpet at fixed flux $\alpha = 1/4$: (a) density of states, **(b)** scaling exponent ν of the DOS with system size, **(c)** the Chern number as a function of E and **(d)** variance of level spacings in the energy-disorder strength plane. Grey rectangles are drawn to guide the eye. We identify energy gaps to be trivial. Regions with quantized values of the Chern number close to 1 are separated by a delocalized state from the Anderson insulator limit (see blue arrow in **(d)**), which is a feature of quantum Hall states. This is in contrast to a direct transition to a fully localized phase for states carrying zero Chern number as a function of W (white arrow in **(d)**). States with $\mathcal{C} \neq 0$ are characterized by a DOS scaling exponent ν smaller than d_H in **(b)**.

2.4 REAL-SPACE FORMULATION OF TOPOLOGICAL INVARIANTS

Due to lack of translational invariance, it is not possible to compute the Chern number directly from the bundle of Bloch occupied bands. Instead, we employ the real-space formula for the Chern number based on an antisymmetric product of projection operators [67]

$$\mathcal{C} = 12\pi \mathrm{i} \sum_{j\in A} \sum_{k\in B} \sum_{l\in C} \left(P_{jk} P_{kl} P_{lj} - P_{jl} P_{lk} P_{kj} \right), \tag{2.5}$$

where $P = |\psi\rangle \langle\psi|$ is the projection operator onto occupied subspace with respect to a given Fermi level E_F and j, k, l label the lattice sites in three distinct neighboring sectors A, B and C arranged in a counterclockwise manner (consult Fig. 2.1). As a remark, for a translationally invariant case Eq. 2.5 reduces to

$$\mathcal{C} = 2\pi \mathrm{i} Tr \left(P \left[[X, P], [Y, P] \right] \right) \tag{2.6}$$

with X and Y being the operators of x and y coordinates, respectively, and the trace is taken over the unit cell.

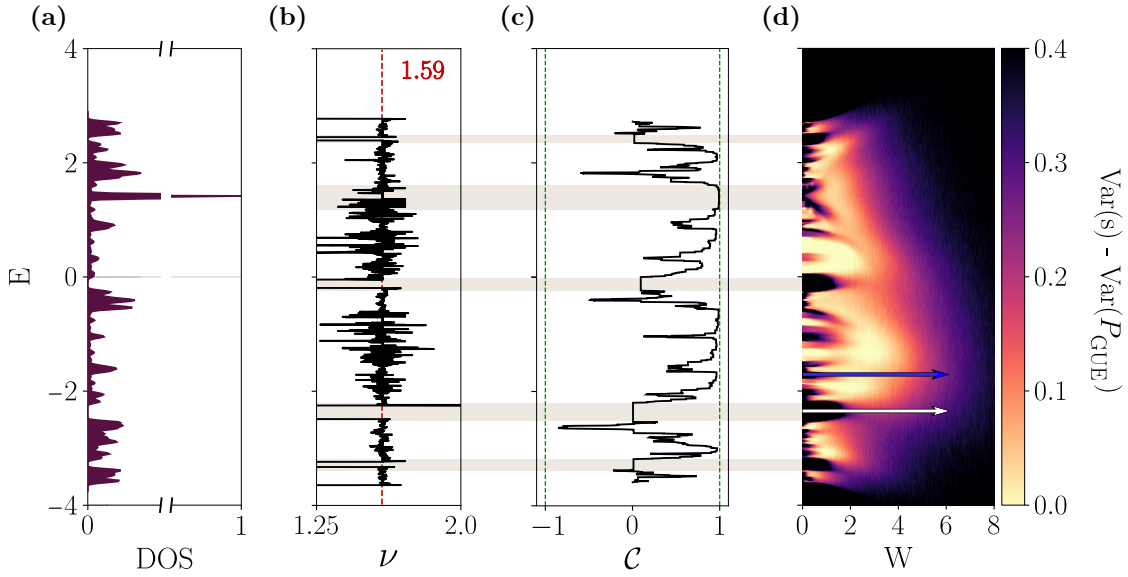

Figure 2.7: Detecting topological properties of Sierpiński gasket at fixed flux $\alpha = 1/4$: (a) density of states, **(b)** scaling exponent ν of the DOS with system size, **(c)** the Chern number as a function of E and **(d)** variance of level spacings in the energy-disorder strength plane. Similar to SC, spectral gaps are also topologically trivial. Quantization of the Chern number is less pronounced, but the levitation and pair annihilation mechanism is still observed (see **(d)**).

The sum in Eq. (2.5) should converge to an integer, when the summation region is large enough. If $\mathcal{C}$ is indeed quantized, it becomes then independent of the detailed choice of A, B, C in the limit of where the number of sites in each part goes to infinity. Using the SC as an example, in Fig. 2.8 we show how a real-space patch choice affects the quantization of $\mathcal{C}$. We compute $\mathcal{C}$ while varying the distance R between the center and the corners of the patch that makes up A, B, C and keeping the aspect ratio of rectangle constant. When the summation region is too small or too large (close to the size of the entire system), $\mathcal{C}$ is far from a non-zero quantized value as expected. We focus on two Fermi levels, $E_F = -1.2$ and $E_F = -1.0$, which correspond to spectral regions with less and more quantized $\mathcal{C}$, respectively. For $E_F = -1.0$, $\mathcal{C}$ is very close to 1 over a large range of R. Conversely, for $E_F = -1.2$, where $\mathcal{C}$ is not quantized, a strong R-dependence is found.

Figs. 2.6 (d), 2.7 (d) present $\mathcal{C}$ as a function of the Fermi energy E at fixed value of flux $\alpha = 1/4$ for the $n = 4$ iteration of SC and the $n = 6$ iteration of the SG with a patch size corresponding to the most robust results. We arrive at following conclusions: (i) All fully gapped regions of the spectrum, for both lattices, carry $\mathcal{C} = 0$, (ii) low DOS regions for the SC in Fig. 2.3 (a) are associated with stable plateaus $\mathcal{C} \sim \pm 1.0$ (for a wide range of energies $E = -1.5 \ldots -0.9$ and $E = 0.9 \ldots 1.5$), as well as less quantized regions with $\mathcal{C} \sim \pm 0.96$ ($E = -2.6 \ldots -2.5$ and $E = 2.5 \ldots 2.6$). Deviations from quantized Chern numbers are observed when the DOS is enhanced, for example around $E = -1.2$ and $E = 1.2$. (iii) Identification of non-trivial regions for the SG is less clear, yet a plateau from $E = 1 \ldots 1.6$ converges to $\mathcal{C} \sim 1.0$.

It is not obvious whether for fractals $\mathcal{C}$ tends to quantized values for almost all energies in the thermodynamic limit, that is the deviation from quantized $\mathcal{C}$ is solely due to finite-size effects. Because of exponential increase in size for every iteration, performing systematic finite-size studies remains challenging. To discuss the connection between the DOS and the Chern number, we calculate the number of states at fixed α averaged over an energy interval $[\epsilon - \delta, \epsilon + \delta]$ (with $\delta = 0.1$ for the SC and $\delta = 0.05$ for the SG) for different system sizes, and

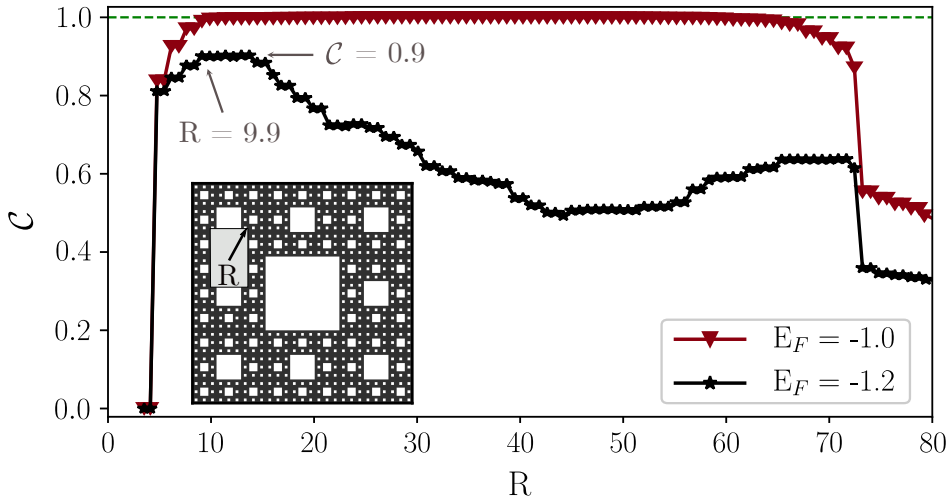

Figure 2.8: Scaling of the Chern number with respect to a real-space patch size: Real-space Chern number calculations for Sierpiński carpet as a function of the half of the diagonal of a rectangular patch R for two Fermi levels $E_F = -1.2$ and $E_F = -1.0$ at fixed flux $\alpha = 1/4$. For spectral regions exhibiting stable plateaus with quantized $\mathcal{C}$, this quantization is observed for a large range of patch sizes. In case of large DOS regions, in which we dominantly observe deviation from a quantized value of $\mathcal{C}$, the value of $\mathcal{C}$ is sensitive to the size and shape of the summation region. $R = 9.9$ corresponds to the size of the patch shown in Fig. 2.1 (a).

compute the average scaling exponent ν of the number of states in that energy range with system size. On average, ν equals the Hausdorff dimension d_{H}. In Fig. 2.6 (b) that for the SC regions with (nearly) quantized Chern number consistently show scaling with $\nu < d_{\mathrm{H}}$. This indicates that the normalized DOS would scale to zero in the thermodynamic limit in regions with quantized Chern number. For the SG, the situation is less clear except in regions of trivial Chern number where no states are found (see Fig. 2.7 (b)).

2.5 EFFECT OF DISORDER

Topological matter is often defined in terms of robustness against disorder. For this reason, we would like to investigate the effect of disorder by adding extra term $\sum_i V_i c_i^\dagger c_i$ to the Hamiltonian in Eq. (2.2), where V_i is drawn from a uniform distribution $[-W/2, W/2]$ and W corresponds to the disorder strength. If the system is characterized by a non-vanishing Hall conductivity, transition to a topologically trivial phase leads to localization of all states at some critical value of disorder, including the protected boundary modes. Disorder-induced topological phase transition is accompanied by a so-called levitation and pair annihilation mechanism [68, 69]. As the disorder increases, the states characterized by non-zero Chern number move towards each other, they meet at intermediate disorder values and annihilate, ultimately leading to Anderson localization at large disorder strength exceeding the band width.

This transition can be captured by level spacing defined as the difference between neighbouring energy levels. For a given energy ϵ and disorder realization $\{V_i\}$, we find two closest eigenvalues satisfying $E_{\lambda,\{V_i\}} < \epsilon < E_{\lambda+1,\{V_i\}}$, then calculate level spacings $s_{\epsilon,m,\{V_i\}} = E_{\lambda+m+1,\{V_i\}} - E_{\lambda+m,\{V_i\}}$, where $m \in \{-k, k\}$, and normalize them. We set $k = 2$ as proposed in Refs. [70, 71] and point out that incorporating differences between further neighbouring levels does not affect the results. Hence, we can study the distribution of the level spacings and the variance $\mathrm{Var}(s_\epsilon) = \langle s_\epsilon^2 \rangle - \langle s_\epsilon \rangle^2$ to determine whether states are

localized or extended. The average is taken with respect m and 10^3 disorder realizations for fixed ϵ. According to the random matrix theory, Hamiltonians with broken time-reversal symmetry are modelled by Gaussian unitary ensemble (GUE). If states are delocalized, then the level spacings should follow the Wigner-Dyson distribution $P_{\mathrm{GUE}}(s) = \frac{32s^2}{\pi^2} e^{-\frac{4}{\pi}s^2}$ with the variance $\mathrm{Var}(P_{\mathrm{GUE}}) = 0.178$. Localized states, on the other hand, are expected to obey the Poisson distribution $P(s) = \exp(-s)$ with a large variance $\sim \mathcal{O}(1)$. Consequently, we use the numerically obtained distribution of the level spacings for several disorder amplitudes W to compute the variance in order to demarcate between localized and delocalized states.

Since disorder calculations require exact diagonalization of the Hamiltonian repeatedly, we consider here smaller systems (iteration $n = 4$ in case of SC and $n = 5$ for SG). This is justified by the fact that fractals exhibit same statistical properties at different scales. In Figs. 2.6 (d) and 2.7 (d), we present the difference between $\mathrm{Var}(s)$ and $\mathrm{Var}(P_{\mathrm{GUE}})$ at fixed flux $\alpha = 0.25$. Regions in energy for which the Chern number is quantized are characterized by a large $\mathrm{Var}(s)$ at small values of W. There are two possible transition scenarios, which can be observed by following a line of increasing W at constant energy, represented by white and blue arrows. Former case corresponds to a direct transition to fully localized system, without $\mathrm{Var}(s)$ ever becoming close to $\mathrm{Var}(P_{\mathrm{GUE}}) = 0.178$. In the latter case, a localized region at small W is separated from the Anderson insulating limit by a delocalized region with $\mathrm{Var}(P_{\mathrm{GUE}}) = 0.178$.

As a cross-check of our calculations, we compare the variances of the level spacings computed over the whole flux range at three different disorder strengths $W = 1, 3, 5$ for regular and fractal lattices (results are illustrated in Figs. 2.9 and 2.10). In case of square and carpet, large variance exactly at $\alpha = 1/2$ is observed as systems become time-reversal invariant.

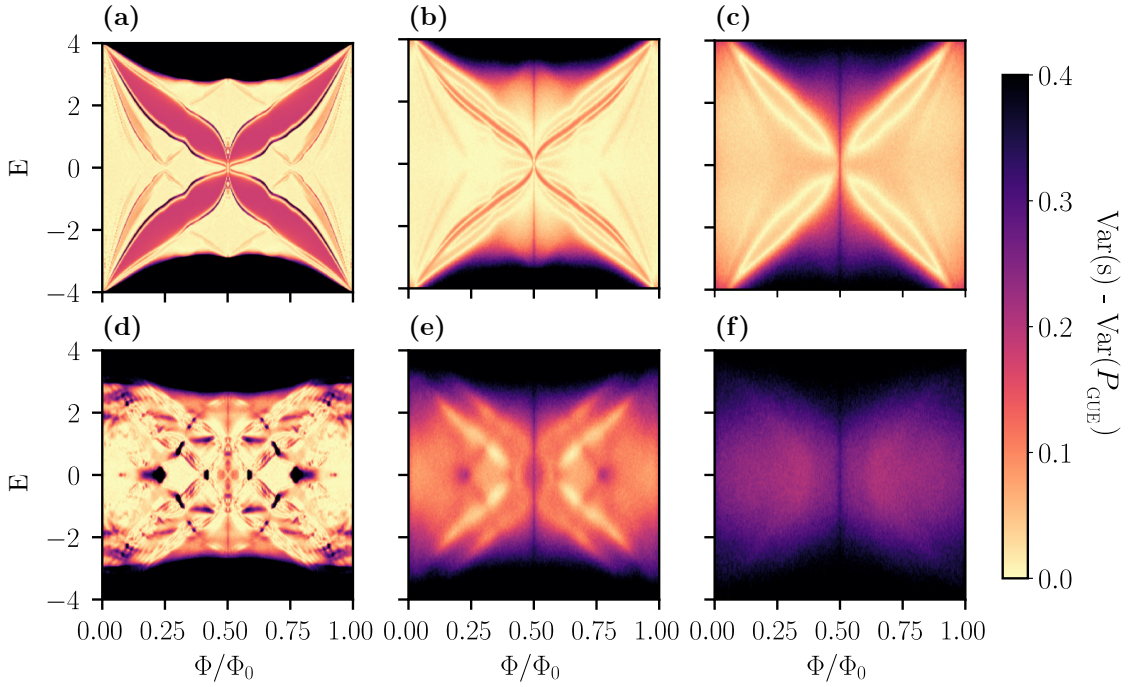

Figure 2.9: Variance of the level spacings for (a, b, c) a square lattice and (d, e, f) the Sierpiński carpet: variances in the energy - flux plane at three disorder strengths, **(a, d)** $W = 1$, **(b, e)** $W = 3$, and **(c, f)** $W = 5$.

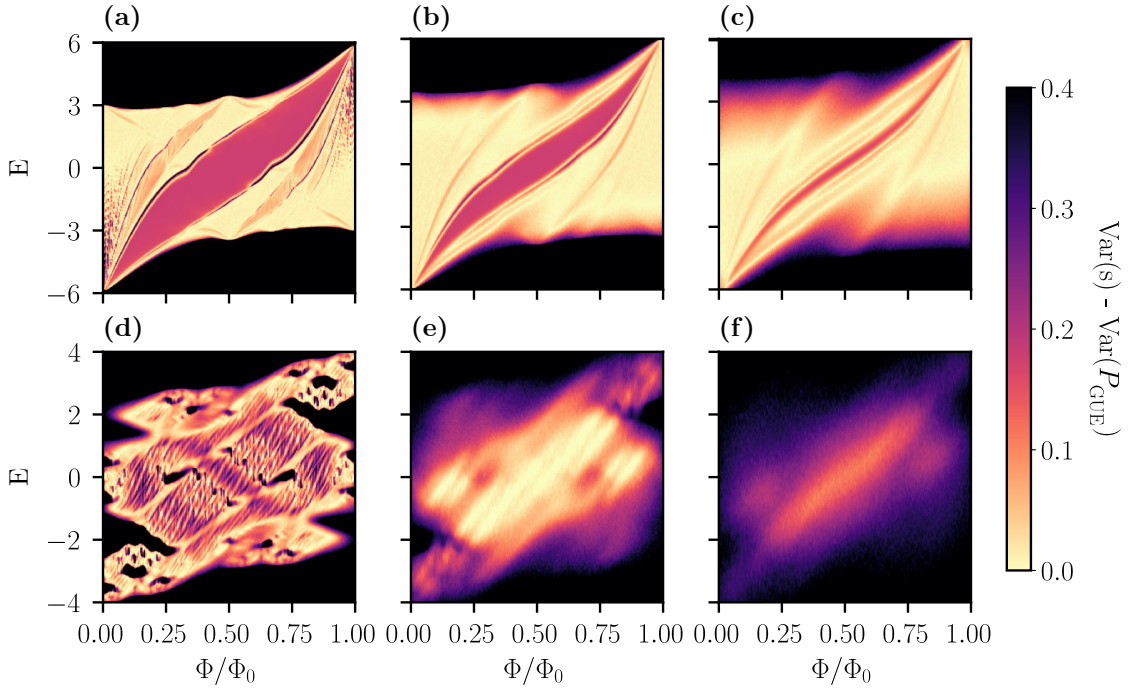

Figure 2.10: Variance of the level spacings for (a, b, c) a triangle lattice and (d, e, f) the Sierpiński gasket: variances in the energy - flux plane at three disorder strengths, **(a, d)** $W = 1$, **(b, e)** $W = 3$, and **(c, f)** $W = 5$.

3

CRYSTAL SYMMETRIES IN GROUP-V MONOLAYERS

What seems to be a natural extension to the ten-fold way is to include spatial symmetries, which are inherently connected to crystalline solids. However, this remains a tedious task due to a large number of possible symmetry configurations (there are 230 space groups in three-dimensions, or 1651 magnetic groups) [72–76].

The presence of crystalline symmetries gives rise to new topological phenomena. Topological crystalline insulators (TCI) are systems in which gapless boundary modes are solely protected by the spatial symmetries. For instance, in the semiconducting bulk SnTe two-dimensional surface states are protected by the mirror symmetry [77, 78] acting non-locally in a real space. Another prominent consequence is the concept of higher-order topological insulators, where non-trivial d-dimensional bulk is accompanied by boundary modes in a $(d-n)$ dimensions, with $n > 1$ [79–81].

A unifying framework of topological quantum chemistry [82] provides a classification based on group theory and local atomic orbitals.

3.1 TOPOLOGICAL CRYSTALLINE INSULATING STATES IN TWO-DIMENSIONAL MONOLAYERS

Despite recent theoretical developments including TCI protected by rotation [83, 84] there are not many material candidates for TCI (planar Bi/Sb with DFT [85]), electron-doped TlM (M = S and Se) (110) monolayer **??**, monolayer and trilayer PbTe [86].

3.1.1 *Liu-Allen tight-binding model*

We employ sp^3 tight-binding model developed in Ref. [**Liu:Allen**] for bulk bismuth and antimony, neglecting hoppings between bilayers as proposed in Ref. [**Murakami:BiQSH**]. Interatomic hoppings are parametrized within the Slater-Koster approach [**Slater:Koster**] and atomic spin-orbit coupling $\lambda \vec{L} \cdot \vec{S}$. The Hamiltonian of the model reads

$$\begin{aligned} H = &\sum_{i,\alpha,\sigma} E_{i\alpha} c^{\dagger}_{i\alpha\sigma} c_{i\alpha\sigma} + \sum_{i,\alpha,\sigma} E^{R,G}_{Field} c^{\dagger}_{i\alpha\sigma} c_{i\alpha\sigma} \\ &+ \Bigg[\sum_{i,j,\alpha,\alpha',\sigma} V_{\alpha\alpha'} c^{\dagger}_{i\alpha\sigma} c_{j\alpha'\sigma} + \frac{\lambda}{3} \sum_{i} (c^{\dagger}_{iz\downarrow} c_{ix\uparrow} - c^{\dagger}_{iz\uparrow} c_{ix\downarrow} \\ &+ i c^{\dagger}_{iz\uparrow} c_{iy\downarrow} + i c^{\dagger}_{iz\downarrow} c_{iy\uparrow} + i c^{\dagger}_{ix\downarrow} c_{iy\downarrow} - i c^{\dagger}_{ix\uparrow} c_{iy\uparrow}) + H.c. \Bigg] , \end{aligned} \tag{3.1}$$

where i, j are lattice indices, $\alpha = \{s, p_x, p_y, p_z\}$ labels orbitals an $\sigma = \{\uparrow, \downarrow\}$ denotes spins. E_i corresponds to the on-site energies and $V_{\alpha\alpha'}$ are the hopping integrals. $E^{R}_{Field} = -E^{G}_{Field} = E_{Field}$ is a perpendicular electric field on $i \in R$ and $i \in G$ sites of two sublattices in a lattice indicated by red and green color in Fig. **??**. The last term is the SOC with a strength λ. According to Chadi [**Chadi**], $1/3$ factor is introduced to renormalized atomic SOC in order to obtain correct SOC splitting of the valence band.

Similarities between Bi and Sb crystals can be seen by looking at Slater-Koster parameters listed in Table I, taken from Ref. [**Liu:Allen**]. Most of the parameters differ by less than

Parameter (eV)	Bi	Sb	Parameter (eV)	Bi	Sb
E_s	-10.906	-10.068	$V'_{sp\sigma}$	0.433	0.478
E_p	-0.486	-0.926	$V'_{pp\sigma}$	1.396	1.418
$V_{ss\pi}$	-0.608	-0.694	$V'_{pp\pi}$	-0.344	-0.393
$V_{sp\sigma}$	1.320	1.554	$V''_{ss\sigma}$	0	0
$V_{pp\sigma}$	1.854	2.342	$V''_{sp\sigma}$	0	0
$V_{pp\pi}$	-0.600	-0.582	$V''_{pp\sigma}$	0.156	0.352
$V'_{ss\sigma}$	-0.384	-0.366	$V''_{pp\pi}$	0	0
λ	1.5	0.6			
a (Å)	4.53	4.30	h (Å)	1.58*	1.64**
d_1 (Å)	3.062	2.902			

Table 3.1: Tight-binding parameters for Bi and Sb taken from Refs. **[Liu:Allen]**, **[stable:bi111]***, **[Sb:nontriv]****. d_1 denotes nearest-neighbor distance between sites in a honeycomb lattice.

15%. The only significant change is in the spin-orbit coupling constant λ, 2.5 times larger in bismuth. Thus, a transition from QSH insulating phase to trivial insulator with increasing x in $Bi_{1-x}Sb_x$ is related, in general, to a decrease of spin-orbit coupling constant.

3.1.2 *Mirror Chern number*

For the case of mirror, the 3Dspace is split in two regions by the mirror plane on whichmirror symmetry acts as an internalZ2symmetry. Thissymmetry can be used to transform the Hamiltonian intoa block-diagonal form where the two blocks are relatedby time-reversal symmetry. Each block separately maybreak time reversal symmetry (class A), hence, we canassign to it a non-vanishing Chern numberCcorrespond-ing to a quantum Hall or Chern insulator phase (the totalChern number of the two blocks is still zero). The result-ing TCI is characterized by mirror Chern numberCinthe corresponding mirror plane.

When $d_z = 0$, a mirror symmetry M_z is restored and TCI phase is exhibited. Recall that mirror Chern number is defined as a difference between Chern numbers corresponding to different mirror-symmetric subsystems:

$$\mathcal{C} = \frac{C_{+M} - C_{-M}}{2} \tag{3.2}$$

3.1.3 *Entanglement measures*

3.1.3.1 *Entanglement entropy*

The concept of the Shannon entropy of a statistical distribution can be extended to the quantum case by defining an entanglement entropy

$$S(\rho) = -Tr(\rho \log \rho) = \sum_i \lambda_i \log \lambda_i \tag{3.3}$$

λ_i are the eigenvalues of ρ (with the assumption that $0 \log 0 \equiv 0$).

3.1.3.2 *Entanglement spectrum*

Calculating entanglement entropy gives a particular number. Therefore, Li and Haldane proposed that the full eigenvalue spectrum of the reduced density matrix may be used to distinguish between phases. This concept has been applied to topological in- sulators, quantum spin chains or quantum Hall fluids. Due to the positivity and Hermiticity, the reduced density matrix ρ_A can be written as follows

$$\rho_A = \frac{1}{Z} e^{-H_{ent}} \tag{3.4}$$

with the partition function $Z = Tr \exp(-H_{ent})$. Hent is the entanglement Hamiltonian and the eigenenergies of Hint are called entanglement spectrum. Thanks to this form of density matrix, the entanglement entropy can be considered as an equivalent to the thermodynamic entropy with a Hamiltonian Hent at temperature T = 1. For a weak entanglement, the gap in spectrum of Hent separates ground state eigenvalue from 'excited states'. In the limit of no entanglement within the system, the gap becomes infinite. A remarkable insight has been made for topological phases in 2 + 1-dimensions, known as an edge-entanglement spectrum correspondence. If the system has edge states (or, in general, possesses low-energy states near an open boundary of the manifold where the system lives), the low-lying edge spectrum of the physical boundary Hamiltonian is an one-to-one correspondence with the low-lying spectrum of Hent

3.1.3.3 *Free-fermionic systems*

Entanglement measures for free fermionic lattice systems can be computed from the two-point correlation function restricted to the subsystem [**Peschel**]

$$C_{ij}^{\alpha\beta} = \mathrm{Tr}\left(\rho_A c_{i\alpha}^{\dagger} c_{j\beta}\right), \tag{3.5}$$

where i, j are lattice indices within the subsystem A and α, β label orbitals or spins. If system is translationally-invariant, the Hamiltonian H can be written in the momentum space with the many-body ground state in a form $|GS\rangle = \prod_{n,k} a_{nk}^{\dagger} |0\rangle$ with operators $a_{nk}^{\dagger}$ corresponding to creation a particle with momentum k and n running over the occupied single-particle Bloch states. Hence, the correlation matrix can be evaluated for each k-point separately via formula $C_{ij}^{\alpha\beta}(k) = \langle GS | c_{i\alpha k}^{\dagger} c_{j\beta k} | GS \rangle$. $C(k)$ is a Hermitian matrix and can be regarded as a spectrally flattened physical Hamiltonian with eigenvalues (denoted by $\{\zeta_k\}$) falling between 0 and 1. Most of the eigenvalues in the spectrum of $C(k)$ lie exponentially close to either 1 or 0, depending whether bulk states are fully localized in the subsystem A or B, respectively, and do not contribute to the entanglement entropy. However, states crossing the partition boundary give rise to non-zero entanglement entropy. If the Hamiltonian describes a topologically non-trivial Z_2 phase in 2D, $C(k)$ will reveal the spectral flow associated with continuous set of intermediate eigenvalues [**Hughes:inv**, **Vish:inv**]. A relation between $\{\zeta_k\}$ and the spectrum of $H_A(k)$ labeled by $\{\xi_k\}$ is following

$$\zeta_k = \left(1 + e^{\xi_k}\right)^{-1}. \tag{3.6}$$

Due to this one-to-one correspondence, we refer to eigenvalues of the correlation matrix as the single-particle entanglement spectrum, which is a conventional practice in the literature [**Alex:CM**, **Vish:inv**, **Hughes:inv**]. Entanglement entropy is then given by

$$S_A = -\sum_a \left(\zeta_a \log \zeta_a + (1 - \zeta_a) \log (1 - \zeta_a)\right), \tag{3.7}$$

where a is index running over all eigenvalues of C. S_A can be calculated [**Ryu:EE**] by summing over the entanglement entropy for each k-point with a normalization factor being the number of unit cells $S_A = 1/N_y \sum_k S_A(k)$.

The number of intersecting branches of edge states in the band structure allows us to distinguish between TI and TCI phases. Similar features can be also observed in entanglement spectra.

3.1.4 *Free-standing layers*

3.1.5 *Substrate effect*

only one pair of modes spectrally connecting o's and 1's is noticed. Hence, we can identify these spectra with TI phase. In order to realize TCI phase in these systems, one needs to find a substrate that weakly couples.

3.2 OBSTRUCTED ATOMIC LIMITS

n general, a set of occupied bands (without strong orfragile topology) can be decomposed into subsets of bandsstemming from localized orbitals at different Wyckoff posi-tions. The minimal subblocks that cannot be further decom-posed areelementary band representations(EBRs), whichare a connected set of subbands induced from placing acertain orbital at a given Wyckoff position .A central statement of TQC is that whenever a set of bands has symmetry properties thatare not compatible with the ones of a sum of EBRs, these bands are topological. In fact, itmeans they cannot be adiabatically connected to an atomic limit with localized orbitals atlattice sites. he topology of a group of bands is entirely character-ized by the symmetry data vectorBcontaining the multiplicity of the various irreduciblerepresentations at different HSPs. Any band structure with symmetry dataBthat satisfies the compatibility relations can always be written as alinear combination of EBRs:

$$B = \sum_i p_i \mathrm{EBR}_i \tag{3.8}$$

where EBRiis the symmetry data vector of theithEBR of the group under consideration,.This decomposition in not generically unique.

3.2.1 *Wannier representation*

For Chern insulators it has been shown that a nonzero Chern number presents a topological obstruction that prevents the construction of exponentially localized WFs [87, 88] (the opposite statement was proved as well [89]). In case of Z_2, there is a topological obstruction only if gauge is chosen in a way that time-reversal symmetry is preserved and Wannier functions come in time reversal symmetric pairs [90].

If system has crystal symmetries as well, obstructions to the Wannier representation does not always guarantee stable topology [91]. There may be systems of an intermediate topological stability, which are characterized by a trivial topological index, but they are not topologically equivalent to a fully insulating limit.

Instead, bands may exhibit a fragile topology which is related to the systems that admit Wannier representation, but may be trivialized to an atomic limit (that is, fully insulating limit) by adding degrees of freedom. Two dimensional fragile topological insulators can

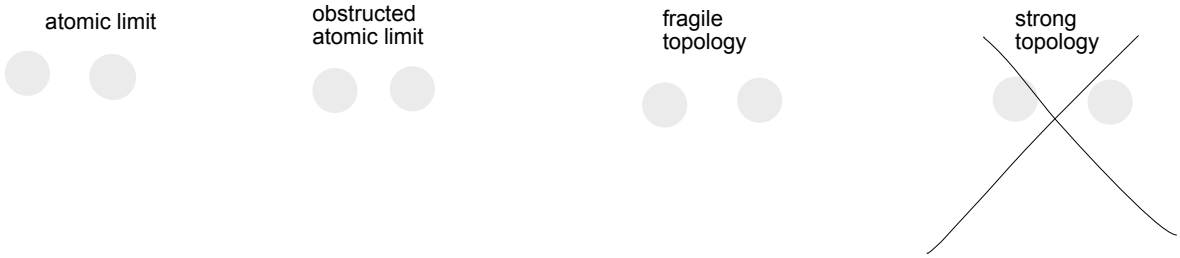

Figure 3.1: In the presence of crystal symmetries, a distinction between topological and trivial phases is less pronounced. Atomic limit corresponds to the situation where Wannier charge centers are located on atomic positions. In case of obstructed atomic limits, Wannier functions are exponentially localized on the Wyckoff positions. Fragile phases cannot be represented in terms of Wannier functions, but a strong index vanishes. Strong topological phases (such as TI or CI) do not admit Wannier representation.

feature boundary states interpolating between conductance andvalence bands. These states, however, lack the robustness of the analogous states in stable topological insulators.Namely, they can be gapped by edge perturbations that preserve the underlying crystalline symmetry.

Surprisingly, a notion of atomic limit becomes not unique - there may be a situation in which the Wannier centers do not coincide with atomic positions (as in the case of trivial atomic limit), but they are rather localized on other symmetric points in the unit cell called the Wyckoff positions.

Quantized fractional corner charges have been predicted as a possible spectral signature for fragile topologicalinsulators in the electronic domain. In a charge neutral system, modes strongly localized at the corners are the counterpart of corner charges.

3.2.2 *Bulk indices*

The key goal was to construct the bulk indices for all layer groups to be sure that boundary effects are related to the nontrivial bulk rather than suitable edge termination.

3.2.2.1 *Symmetry indicators*

The Fu-Kane parity criterion for inversion-symmetric topological insulators given in Eq. 1 is a special case of more general framework of symmetry indicators [92]. Band topology is defined b, with a further extension to superconductors [93]. Symmetry indicators are particularly suitable in a search for real materials as they can be easily employed for ab initio results.

Topological band structures arise whenever there is a mismatch between momentum-space and real-space solutions to symmetry constraint

3.2.2.2 *Wilson loops*

Non-trivial topology can be captured by the Berry phases of the bands under consideration. Non-Abelian Wilson loops are a generalization of Berry phase for multi-band system

$$W[\gamma] = \bar{\text{exp}}\left(\oint_{gamma} d\ell A(\mathbf{k})\right) \tag{3.9}$$

where $\bar{\text{exp}}$ path ordering such that operators at the beginning ofthe path appear to the right of operators at the end.

$$W_\gamma = \prod_{\mathbf{k}} P(\mathbf{k}) \tag{3.10}$$

The Wilson loop operator satisfies $W_\gamma W_\gamma^\dagger = P(k^*)$ and so, since any projector satisfies $[P(k)]^2 = P(k)$, its eigenvalues are either zero or of the form $e^{i\theta_\alpha^\gamma}$, $\alpha = 1 \dots N$. In the following, we refer to the set of $\{\theta_\alpha^\gamma\}_{\alpha=1\dots N}$ as the Wilson loop spectrum, suppressing the zero eigenvalues. The phases of these eigenvalues (Wilson spectrum) are related to the spectrum of the position operator projected on the space of bands below the gap [94]. Wilson loops can be computed efficiently numerically by employing a discretized version:

$$W[\gamma] = F_{\mathbf{k}_0,\mathbf{k}_1} F_{\mathbf{k}_1,\mathbf{k}_2} \dots F_{\mathbf{k}_{p-1},\mathbf{k}_p} \tag{3.11}$$

with $\mathbf{k}_0 = \mathbf{k}_p$ and $F^{m,n}_{\mathbf{k}_i,\mathbf{k}_j} =$

The eigenvalues of W along any non-contractible loop γ defines a map $S^1 \to S^1$. In the presence of crystalline symmetries, their winding number can serve as topological index. The presence of crystalline symmetries imposes constraints on the Wilson loop spectrum

The anti-unitary TRS $\mathcal{T}$ acts on the Bloch Hamiltonian as $\mathcal{T}\mathcal{H}(k)\mathcal{T}^{-1} = \mathcal{H}(-k)$. For the projectors this implies $\mathcal{T}P(k)\mathcal{T}^{-1} = P(-k)$. When γ is mapped onto itself by TRS, and its starting point satisfies $k^* = -k^*$ up to a reciprocal lattice vector, we then have

$$\mathcal{T}W_\gamma\mathcal{T}^\dagger = \prod_k^\gamma P(-k) = W_\gamma^\dagger. \tag{3.12}$$

Due to $\mathcal{T}$ being anti-unitary and $\mathcal{T}^2 = -1$, this implies a Kramers degeneracy of the Wilson loop spectrum, i.e., every θ_α^γ is (at least) two-fold degenerate when γ is mapped onto itself by time reversal.

Now, if there is a crystal symmetry $\mathcal{S}$ that reverses the direction of γ and leaves the starting point invariant so that $k^* = \mathsf{S}k^*$ up to a reciprocal lattice vector, we have

$$\mathcal{S}W_\gamma\mathcal{S}^\dagger = \prod_k^\gamma \left[\mathcal{S}P(k)\mathcal{S}^\dagger\right] = W_\gamma^\dagger. \tag{3.13}$$

Since $\mathcal{S}$ is unitary, the Wilson loop is unitarily equivalent to its complex conjugate and so its eigenvalues come in complex conjugated pairs. This implies a symmetry of the Wilson loop spectrum around $\theta = 0$, for every θ_α^γ there is a corresponding $-\theta_\alpha^\gamma \mod 2\pi$.

he calculation of Berry phasesof reduced sectors within the subspace of occupied en-ergy bands. To find the relevant subspace we resolve theenergy bands into spatially separated "Wannier bands"through a Wilson-loop calculation, or equivalently, a di-agonalization of a ground state projected position oper-ator. We call this structure 'nested Wilson loops'. At its core, this nested Wilson loopstructure reflects the fact that even gapped edges of topo-logical phases can signal a non-trivial bulk-boundary cor-respondence when the gapped edge Hamiltonian is topo-logical itself and inherits such non-trivial topology fromthe bulk. We may furthermore employ nested Wilson loops [**BABHughesBenalcazar17**, 95]. Let $W_i(k_j)$, $i \neq j$, denote the Wilson loop along the noncontractible loop $\gamma : (k_i = 0, k_j) \to (k_i = 2\pi, k_j)$, where (k_i, k_j) labels a point in the two-dimensional BZ in some basis (chosen such that $k_{i,j} = 0$ and $k_{i,j} = 2\pi$ are related by reciprocal lattice vectors). Consider the Wilson loop Hamiltonian $H_{W_i}(k_j)$, defined by

$$\left[e^{iH_{W_i}(k_j)}\right]_{mn} = \langle u_m(k_i = 0, k_j)|\, W_i(k_j)\, |u_n(k_i = 0, k_j)\rangle\,. \tag{3.14}$$

Equations (3.12) and (3.13) then imply

$$\begin{aligned} \mathcal{T}_{k_j} H_{W_i}(k_j) \mathcal{T}_{k_j}^\dagger &= H_{W_i}(-k_j), \\ \mathcal{S}_{k_j} H_{W_i}(k_j) \mathcal{S}_{k_j}^\dagger &= -H_{W_i}(\mathsf{S}k_j), \end{aligned} \tag{3.15}$$

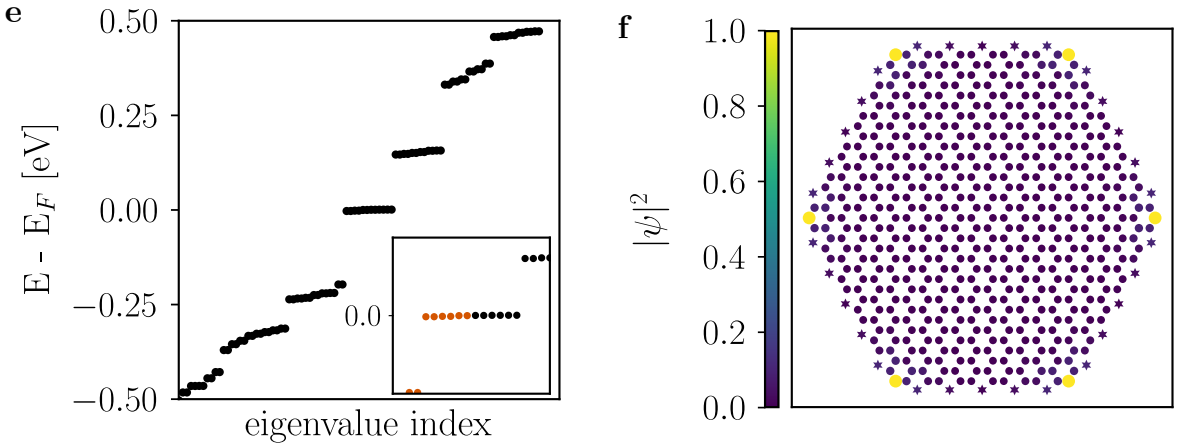

Figure 3.2: Low-energy spectrum of a finite armchair-terminated flakeof the 3cOAL. The inset presents the energies around the Fermi level, with filled states in orange. (f) The electronic densities of the cornerstates with color scale proportional to the normalized square modulus of the eigenstates $|\psi|^2$ (normalized with respect to the largest $|\psi|^2$).The tellurium atoms used for edge passivation are shown as stars.

where we defined

$$\begin{aligned}\left(\mathcal{T}_{k_j}\right)_{mn} &= \langle u_m(-k_j)|\,\mathcal{T}\,|u_n(k_j)\rangle\,,\\ \left(\mathcal{S}_{k_j}\right)_{mn} &= \langle u_m(\mathsf{S}k_j)|\,\mathcal{S}\,|u_n(k_j)\rangle\,.\end{aligned} \tag{3.16}$$

We see that $\mathcal{T}$ implies a TRS of the Wilson loop Hamiltonian, whereas $\mathcal{S}$ implies a particle-hole symmetry. These properties are needed for the definition of quantized topological invariants of the *nested Wilson loop*: We define W_i^{b} as the Wilson loop calculated from a gapped set eigenstates b of $H_{W_i}(k_j)$ along a closed, non-contractible path $k_j : 0 \to 2\pi$ in the reduced BZ.

3.2.3 *Fractional corner charges in finite flakes*

Predicted also in atomically thin carbon allotrope called graphdiyne [96, 97].

They share the very same crystal structure. With non-zero buckling, these systems preserve C_3 and $\mathcal{I}$.

I

We present the band representations of the space groups 164 ($P\bar{3}m1$) and 191 ($P6/mmm$) relevant for discussed materials. To deduce Wyckoff positions from which EBRs can be induced, we use data collected from the Bilbao Crystallographic Server [82, 98–100]. Note that we discard Wyckoff positions with nonzero z-component as they are irrelevant for a 2D geometry. The irreducible representations of bands at high-symmetry points were obtained using the `irrep` code [**irrep-github**], which relies on the double space group character tables [**elcoro2017**] published on the Bilbao Crystallographic server [**bilbao-server**].

SG	phase	band representation	EBRs
164	TI 1	$(3\bar{\Gamma}_8 \oplus 2\bar{\Gamma}_9, 2\bar{M}_3\bar{M}_4 \oplus 3\bar{M}_5\bar{M}_6, 2\bar{K}_4\bar{K}_5 \oplus 3\bar{K}_6)$	-
164	TI 2	$(2\bar{\Gamma}_8 \oplus 2\bar{\Gamma}_9 \oplus \bar{\Gamma}_4\bar{\Gamma}_5, 2\bar{M}_3\bar{M}_4 \oplus 3\bar{M}_5\bar{M}_6, 2\bar{K}_4\bar{K}_5 \oplus 3\bar{K}_6)$	-
164	$3c$ OAL	$(3\bar{\Gamma}_8 \oplus \bar{\Gamma}_9 \oplus \bar{\Gamma}_4\bar{\Gamma}_5, 2\bar{M}_3\bar{M}_4 \oplus 3\bar{M}_5\bar{M}_6, 2\bar{K}_4\bar{K}_5 \oplus 3\bar{K}_6)$	$\bar{E}_1(2d) \oplus {}^1\bar{E}_g^2\bar{E}_g(3c)$
164	$1a$ OAL	$(2\bar{\Gamma}_8 \oplus 2\bar{\Gamma}_9 \oplus \bar{\Gamma}_4\bar{\Gamma}_5, 3\bar{M}_3\bar{M}_4 \oplus 2\bar{M}_5\bar{M}_6, 2\bar{K}_4\bar{K}_5 \oplus 3\bar{K}_6)$	$\bar{E}_{1g}(1a) \oplus \bar{E}_{1u}(1a) \oplus \bar{E}_1(2d) \oplus {}^1\bar{E}_g^2\bar{E}$
191	TCI	$(\bar{\Gamma}_7 \oplus \bar{\Gamma}_8 \oplus \bar{\Gamma}_9 \oplus \bar{\Gamma}_{11} \oplus \bar{\Gamma}_{12}, 3\bar{M}_5 \oplus 2\bar{M}_6, 2\bar{K}_7 \oplus \bar{K}_8 \oplus 2\bar{K}_9)$	-

Table 3.3: Band representations corresponding to distinct phases as shown in Fig. **??** in the main text. '-' indicates that a given band representation cannot be written as a combination of EBRs.

phase	$\#\Gamma_2^{\mathcal{I}}$	$\#M_2^{\mathcal{I}}$	$[M_2^{\mathcal{I}}]$	$\#\Gamma_2^{(3)}$	$\#K_2^{(3)}$	$[K_2^{(3)}]$	$\chi_{\mathcal{I}}^{(3)} = ([M_2^{\mathcal{I}}], [K_2^{(3)}])$	Δ_{TI}
TI 1	4	6	2	0	4	4	(2, 4)	1
TI 2	4	6	2	2	4	2	(2, 2)	1
$3c$ OAL	2	6	4	2	4	2	(4, 2)	0
$1a$ OAL	4	4	0	2	4	2	(0, 2)	0

Table 3.2: Topological invariants and symmetry indicators $\chi_{\mathcal{I}}^{(3)}$ corresponding to different regions in the phase diagrams: The symmetry indicators were calculated using the primitive 2-site unit cell of the honeycomb lattice (see Table 3.3 for a decomposition in terms of elementary band representations). The indices $\chi_{\mathcal{I}}^{(3)}$ allow for a more refined classification even of the strong TIs. We find that the $3c$ and $1a$ OALs differ in their inversion indicator $[M_2^{\mathcal{I}}]$ and thus, as explained in the main text, inversion-symmetric flakes built from their hexagonal unit cells differ by a protected corner charge equal to 1 mod 2.

4

TOPOLOGY IN NON-HERMITIAN SYSTEMS

In quantum mechanics, the condition that the observable must be a Hermitian operator has a deep physical reasoning - the corresponding expectation value has to be a real-valued number. However, this strong assumption can be relaxed - it is possible to have a non-Hermitian operator with real spectrum. This observation gave rise to the concept of PT-symmetric Hamiltonians, where the real spectrum is guaranteed by the product of parity and time-reversal symmetries [101].

Another motivation comes from the open systems. Instead of a full treatment with Lindblad formalism, for instance, nH Hamiltonians can effectively capture the coupling of the system with its environment, where the non-Hermiticity models the gains and losses.

Such system exhibits interesting phenomena without Hermitian counterpart: exceptional points, the skin effect and, as a consequence, the breakdown of bulk-boundary correspondence.

Novel features of nH systems are seen at the level of 2×2 matrices. Consider a matrix M: M =

$$\begin{pmatrix} 0 & \alpha \\ 1 & 0 \end{pmatrix} \tag{4.1}$$

If $\alpha \neq 1$, M is not diagonalizable, and only admits the Jordan block form. NH matrices have distinct left- and right- eigenvectors. Therefore, a remedy for some problems may be to consider quantities of interests within the biorthogonal quantum mechanics. For instance, the norm is then given by the inner product between left and right eigenvectors. This attempt allowed to restore BB correspondence in some models. Another way is to consider the singular value decomposition (SVD) instead of eigenvalue problem. However, the interpretation of the singular values is not physical (in contrast to the eigendecomposition, where the eigenvalues are the energies) [102].

In non-Hermitian case, the topology is already manifested in single-band systems (in contrast to Hermitian systems where at least two bands are needed). Also, the winding number for 1D systems is defined through the eigenvalues, not the eigenstates.

4.1 BREAKDOWN OF BULK-BOUNDARY CORRESPONDENCE

As Hermitian conjugate is not longer equal to complex conjugate and transpose, different type of symmetries appear. Classification, firstly by [103], extended recently in Refs. [104–106]

4.2 EXCEPTIONAL POINTS

Let us remind the concept of Weyl points. Consider the Hamiltonian in 3D

$$H = \mathbf{k} \cdot \boldsymbol{\sigma} = k_x \sigma_x + k_y \sigma_y + k_z \sigma_z. \tag{4.2}$$

This model exhibits a robust generic degeneracy. As all σ_i are used, adding other term proportional to σ_i only shifts the touching point. Now compare the following model in 2D:

$$H = k_x \sigma_x + k_y \sigma_y + ir\sigma_y \tag{4.3}$$

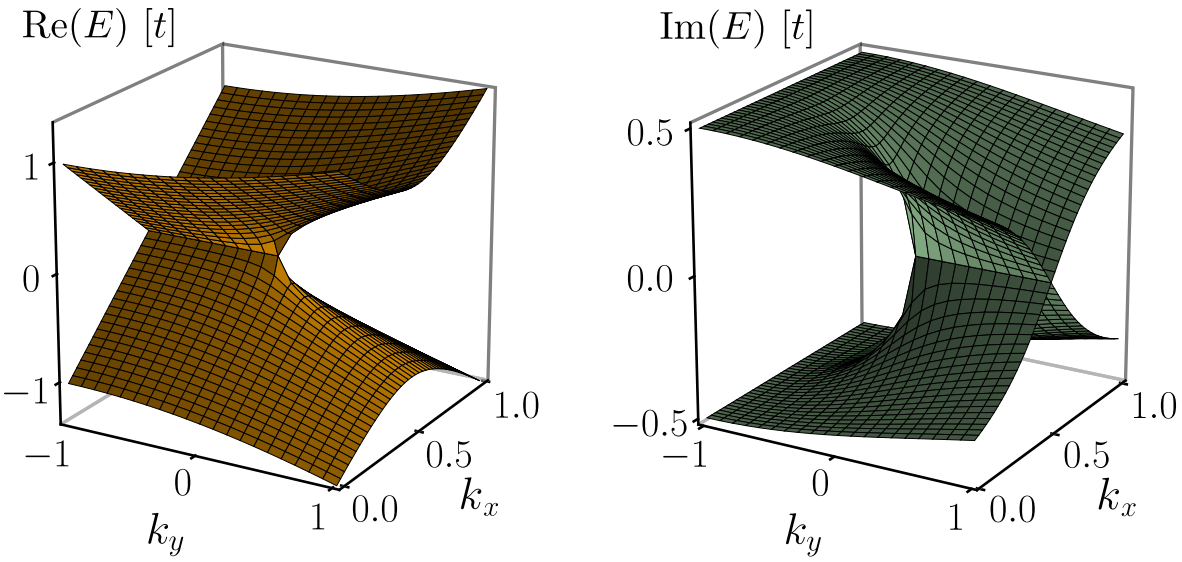

Figure 4.1: Real (left) and imaginary (right) part of the spectrum of the Hamiltonian defined by Eq.(4.3). Gapless region of real part of the spectrum corresponds to gapped imaginary spectrum and vice versa.

Non-zero r gives rise to the degeneracies in non-Hermitian band structure called exceptional points. Exceptional points can be seen as equivalents of Weyl nodes as they appear in generic points in k-space and one has to get them closer to annhilate them (for example by adding very large mass term).

4.2.1 *π-flux model*

To underline the generality of our arguments, we will present the theory in the language of (non-Hermitian) tight-binding Hamiltonians, which may represent either a quantum system or the dynamical matrix and response function of a classical system. We start our considerations with the π-flux tight-binding model on a square lattice. It is characterized by a nearest-neighbor hopping t, where exactly one of the four sides of each plaquette has a negative hopping amplitude compared to the three others. These hoppings require a unit cell of two plaquettes of the square lattice [see Fig. **??** a)]. The Bloch Hamiltonian for a system with periodic boundary conditions (PBC) in x and y directions, yielding the momenta k_x and k_y, can be written as

$$H_{\text{ß}}(k_x, k_y) = t \begin{pmatrix} 2\cos k_y & 1 + e^{-ik_x} \\ 1 + e^{ik_x} & -2\cos k_y \end{pmatrix}. \tag{4.4}$$

The model has two Dirac-like band touchings at momenta $(k_x, k_y) = (\pi, \pi/2)$ and $(k_x, k_y) = (\pi, 3\pi/2)$ [see Fig. **??** a) for the band structure].

We add a non-Hermitian (gain/loss) term as a diagonal hopping through one of the plaquettes in the unit cell [see Fig. **??** a)]. It assigns a complex amplitude ir (with r a real number) to the the process of a particle hopping along the diagonal toward the upper right, and the exact same amplitude ir to the reversed process. Hermiticity would require that the latter process has the complex conjugated amplitude $-ir$. As such, the addition

$$H(k_x, k_y) = H_{\text{ß}}(k_x, k_y) - ir \begin{pmatrix} 0 & e^{ik_y} \\ e^{-ik_y} & 0 \end{pmatrix} \tag{4.5}$$

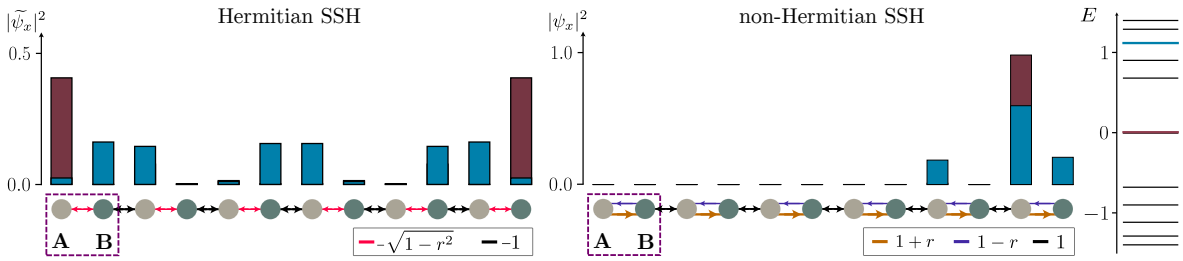

Figure 4.2: Relation between the Hermitian ($r = 0$) and non-Hermitian ($r = 0.9$) dimerized chain, the SSH model. The spectrum of both models is equal with open boundary conditions, including SSH-type end states. However, *all* states in the non-Hermitian model are localized on one side of the system. The amplitude at each lattice site for the two eigenstates marked in the spectrum on the right are plotted with the respective color.

violates Hermiticity for this diagonal hopping process. Despite its non-Hermiticitiy, the model still is reciprocal, as it satisfies $H(k_x, k_y) = H^{\mathsf{T}}(-k_x, -k_y)$ under transposition.

Hamiltonian (4.5) has two complex-valued eigenbands with remarkable properties: they touch (i. e. the two eigenvalues have equal real and imaginary part) in two pairs of points. Upon introducing a finite r, the Dirac points of the original π-flux model each split into a pair of these points. Such degeneracy points in non-Hermitian systems are called exceptional points and are the generic band touchings in a space with two parameters (here, k_x and k_y). The band structure in the vicinity of an exceptional point is illustrated in Fig. **??** b).

We proceed to consider Hamiltonian (4.5) with OBC in x-direction, which leaves $k_y \in [0, 2\pi]$ well defined as a boundary momentum, and define $\tilde{H}(k_y)$ as the Hamiltonian for the strip geometry. While $\tilde{H}^{\top}(k_y) = \tilde{H}(-k_y)$ guarantees reciprocity of the full system, each instance of $\tilde{H}(k_y)$ *locally* breaks reciprocity for a fixed k_y when seen as a purely one-dimensional model, except for $k_y = -k_y \mod (2\pi)$. The effective 1D model for a given k_y exhibits the non-Hermitian skin effect as discussed in Refs. [107, 108]: The eigenstates of a Hermitian system form an orthonormal basis whose squared amplitudes, when summed over all states, are equal on all lattice sites. In a non-Hermitian system this need not be the case, since right (left) eigenstates of a non-Hermitian matrix do not individually form an orthonormal basis. As a result, they can all be localized at only one edge of the system, which defines the skin effect. In our model, the skin effect is realized due to the term proportional to r in Eq. (4.5), which renders the hopping probability for going right different from the probability for going left. This leads to an accumulation of *all eigenstates* towards only one edge.

We expand the Hamiltonian (2) to linear order in the momentum deviations δk_y around these two points and in r [i. e. we drop a term $\mathcal{O}(r\,\delta k_y)$]. Denote by $H^{(\pm)}_{x\alpha,x'\alpha'}(\delta k_y)$ the matrix elements for the thus expanded strip Hamiltonian, where $x, x' = 1, \cdots, L$ labels the unit cell across the strip and $\alpha, \alpha' \in \{1, 2\}$ refers to the two sublattices. We will now show that, under OBCs but *not* PBCs, this non-Hermitian Hamiltonian is related, by *non-unitary* transformations, to a pair of well-known Hermitian Hamiltonians. Our discussion closely follows Ref. [107]. The transformation (setting $t = 1$)

$$O^{(\pm)}_{x,x'} = \delta_{x,x'} \left(\sqrt{\frac{1 \mp r}{1 \pm r}} \right)^{x} M^{(\pm)}(r), \tag{4.6}$$

with $M^{(\pm)}(r)$ an appropriate 2×2 nonsingular matrix acting on the sublattice space, maps $\tilde{H}^{(\pm)}(\delta k_y) = \left(O^{(\pm)}\right)^{-1} H^{(\pm)}(\delta k_y) O^{(\pm)}$, with

$$\begin{aligned} \tilde{H}^{(\pm)}_{x,x'}(\delta k_y) = \delta_{x,x'} \begin{pmatrix} 2\delta k_y & -\sqrt{1-r^2} \\ -\sqrt{1-r^2} & -2\delta k_y \end{pmatrix} \\ - \begin{pmatrix} 0 & \delta_{x',x+1} \\ \delta_{x',x-1} & 0 \end{pmatrix}. \end{aligned} \tag{4.7}$$

For $\delta k_y = 0$, Eq. (4.7) is the tight-binding Hamiltonian for a dimerized chain, known as the Su-Schrieffer-Heeger model [see Fig. 4.2)]. For $-1 < r < 1$, $r \neq 0$, the chain is bulk insulating but has one SSH-type midgap state localized at each end of the chain. Its bulk states are of delocalized Bloch character, while the end states are exponentially localized with a ratio $\tilde{\psi}_{x,\alpha}/\tilde{\psi}_{x\pm1,\alpha} = \sqrt{1-r^2}$ of wave function amplitudes on neighboring lattice sites. [We denote by by $\psi_{x,\alpha}(\delta k_y)$ and $\tilde{\psi}_{x,\alpha}(\delta k_y)$ the eigenstates of $H^{(\pm)}(\delta k_y)$ and $\tilde{H}^{(\pm)}(\delta k_y)$, respectively.] Finite but small δk_y mainly has the effect of lifting the degeneracy of the SSH-type end states from eigenvalue 0 to $\pm 2\delta k_y$.

Being related by $O^{(\pm)}$, $\tilde{H}^{(\pm)}(\delta k_y)$ and the non-Hermitian Hamiltonian $H^{(\pm)}(\delta k_y)$ are isospectral, but their eigenstates differ in important ways. The x-dependent factor in $O^{(\pm)}$ turns *all* the Bloch-type bulk states into exponentially localized states, with $\psi_{x,\alpha}/\psi_{x\pm1,\alpha} \approx \sqrt{2/(1 \pm r) - 1}$ – which is a stronger exponential decay than that of the SSH-type end states. Whether the localization is on the left or right edge of the system depends on the sign of r and is opposite for $H^{(+)}(\delta k_y)$ and $H^{(-)}(\delta k_y)$. We conclude that on a strip geometry all eigenmodes of the model Eq. (2) are localized on one side of the sample for $k_y \sim \pi/2$ and on the opposite side for $k_y \sim 3\pi/2$. This constitutes the *reciprocal skin effect*, enabled by the non-Hermiticity of the Hamiltonian. Reciprocity enforces the opposite localization at opposite momenta k_y.

4.3 SKIN EFFECT

nH Hamiltonians are sensitive to the boundary conditions. Eigenstates localization properties may change dramatically. All states for the system in an open geometry may be exponentially localized on the one edge, which is dubbed the skin effect (note: this has nothing in common with a typical skin effect, where the electrons in a conductor prefer to flow far from the middle due to electron-electron repulsion).

Previously, it was known that the skin effect can be induced by having unbalanced directed hoppings. However, this breaks the reciprocity, defined as

$$H(k) = H^T(-k) \tag{4.8}$$

4.3.1 *Reciprocal skin effect*

Here, we show that in two- or higher-dimensions it is possible to have the skin effect with the condition defined by Eq. (4.8).

SUMMARY

Recent years have witnessed an immense interest in finding and exploring topological materials, both from theoretical and experimental perspectives, as they hold great promise for technological applications ranging from the electronics to quantum computing. In this thesis, we have studied three different classes of topological phases that fall beyond the well-established classification of topological insulators and superconductors.

In Chapter 2, we have discussed the realization of topological phases in fractal geometries with a non-integer Hausdorff dimension. By means of a case study, we investigated the properties of Sierpiński carpet and gasket in a homogeneous magnetic field. A key finding is that characteristic features of quantum Hall systems in two dimensions are also observed in *almost* two-dimensional lattice models. Therefore, it is imperative to ask what dimensional and connectivity properties a graph must have in order to support topological states. Obtained results call for an extension of the ten-fold way to more general graphs and impose a question about the bulk-boundary correspondence in systems without a sharp distinction between the bulk and the edge. An interesting research direction would be to provide a systematic classification for scale-invariant systems and define topological invariants in analogy to Bloch-type invariants for models with translational invariance.

In Chapter 3, a notion of obstructed atomic limits has been introduced. To support our theoretical findings, we proposed monolayers of bismuth, antimony and arsenic as material candidates. High-throughput calculations combining density functional theory and machine learning algorithms have been already performed, but mostly for bulk materials. Hence, it would a useful (and challenging) task to carry out large-scale computations for two-dimensional OALs.

Finally, in Chapter 4 we have studied models defined by non-Hermitian Hamiltonians. In particular, we demonstrated experimentally the *reciprocal* skin effect using a topolectrical platform. Despite rapid development in this field, there are several not fully explored directions. One of them is the interplay between non-Hermiticity and interactions. Conceivably, there may be a way to construct non-Hermitian topologically ordered states without Hermitian counterparts.

A

BAND THEORY

If the crystal potential $V(\mathbf{r})$ is periodic

$$V(\mathbf{r}+\mathbf{R}) = V(\mathbf{r}), \tag{A.1}$$

then, according to the Bloch theorem, the eigenstate of the H can be written in a form of plane waves

$$\psi_{n,\mathbf{k}}(\mathbf{r}) = e^{-i\mathbf{k}\cdot\mathbf{r}} u_{n,\mathbf{k}}(\mathbf{r}) \tag{A.2}$$

A.0.1 *General definitions*

This imposes only quadratic terms in creation and annihilation operators in the second-quantized Hamiltonian. We define a crystal as a regular arrangement of the unit cells at positions $\mathbf{R_n}$

$$\mathbf{R_n} = n_1\mathbf{a}_1 + n_2\mathbf{a}_2 + n_3\mathbf{a}_3, \quad i = 1, 2, 3 \quad \text{and} \quad \mathbf{n} = (n_1, n_2, n3) \in \mathbb{R}^3 \tag{A.3}$$

where $\{\mathbf{a}_i\}$ are the linearly independent basis vectors. We can define the reciprocal lattice vectors $\{\mathbf{b}_i\}$

$$\mathbf{G}_m = m_1\mathbf{b}_i + m_2\mathbf{b}_i + m_3\mathbf{b}_i, \quad m_i \in \mathbb{Z} \tag{A.4}$$

satisfying

$$\mathbf{a}_i \cdot \mathbf{a}_i = 2\pi\delta_{ij}, \quad i, j = 1, 2, 3 \tag{A.5}$$

constructed

$$\mathbf{b}_i = 2\pi\frac{\mathbf{a}_j \times \mathbf{a}_k}{\mathbf{a}_i \cdot (\mathbf{a}_j \times \mathbf{a}_k)} \quad \text{and} \quad \mathbf{a}_i = 2\pi\frac{\mathbf{b}_j \times \mathbf{b}_k}{\mathbf{b}_i \cdot (\mathbf{b}_j \times \mathbf{b}_k)} \tag{A.6}$$

$$\mathbf{R}_n \cdot \mathbf{G}_m = 2\pi\,(n_1m_1 + n_2m_2 + n_3m_3) = 2\pi N, \tag{A.7}$$

with N being an integer.

Brillouin zone is the unit cell of the reciprocal lattice.

A.0.2 *Group theory: representations and character table*

Here, we recall basic notions from group theory [109]. A group $\mathbb{G}$ has the properties:

- the product of two elements of $\mathbb{G}$ is also in $\mathbb{G}$: $a, bin\mathbb{G} \Rightarrow a \star b = c \in \mathbb{G}$
- there is a unit element $e \in \mathbb{G}$ that satisfies $e \star a = a \star e = a, \forall a \in \mathbb{G}$
- multiplication is associative: $a \star (b \star c) = (a \star b)\star$
- for every element $a \in \mathbb{G}$, there is an inverse $a^{-1} \in \mathbb{G} \Rightarrow a^{-1} \star a = a \star a^{-1} = e$.

A group is call Abelian if for all elements $a \star b = b \star a$, otherwise it it non-Abelian.

The group G describing symmetry operations that leaves a crystal invariant is called a space group. An operator T_g corresponding to certain symmetry operation $g \in G$ commutes with the matrix of the Hamiltonian, i.e. $[T_g, H] = 0$. In reciprocal space, although the whole

matrix H still commutes with T_g, a block $H(k)$ corresponding to a vector k in the BZ may not do so:

$$T_g H(k) T_G^+ = H(gK) \tag{A.8}$$

in Wigner-Seitz notation $g = \{R|\mathbf{v}\}$. The set of $g \in G$ that leaves k invariant up to a reciprocal lattice vector G is called little group G_k of k:

$$G_{\mathbf{k}} = \{g = \{p_g|\mathbf{r}_g\} \in G|p_g\mathbf{k} \approx \mathbf{k} \tag{A.9}$$

whereGis the crystal space group,pgis the point group part ofG,rgis the translation part ofG, andindicatesequivalence modulo translation by integer multiples of reciprocal lattice vectors. Note thatGkcontains all thetranslation symmetries. Topological quantum chemistry (TQC) (10,24) maps this momentum space description to areal space picture and offers simple criteria to asses the topology of a set of bands.

Consider a set of eigenstates $H(\mathbf{k})$. Under the action of a symmetry operation $g \in G_{\mathbf{k}}$, each $|\psi_{n\mathbf{k}}\rangle$ transforms linearly

$$gket\psi_{i\mathbf{k}} = \sum_{j=1}^{N} K^{ji}(g)\,|\psi_{j\mathbf{k}}\rangle \tag{A.10}$$

Matrices $K(g)$ form the representation K of $G_{\mathbf{k}}$ defined in the space spanned by $\{|\psi_{n\mathbf{k}}\rangle\}_N$. It is said that K is an IR, if this space can not be divided in smaller invariant non-trivial subspaces. Every IR is characterized by the set of traces $\chi_K(g) = TrK(g)$ of its matrices, known as character of the IR. Eigenstates $|\psi_{n\mathbf{k}}\rangle$ transform under IRs of $G_{\mathbf{k}}$

A Wyckoff position is a generic location inside the unit cell of a crystal. Each Wyckoff positionw has its own site-symmetry group G_w which is a subgroup of the crystal space group$G$:

$$G_w = \{g = \{p_g|\mathbf{r}_g\} \in G| \tag{A.11}$$

Among all points inside the unit cell, maximal Wyckoff positions play an important role. These are defined as sites where the site-symmetry group is a maximal subgroup of G

$$H|G_w \subset H \subset G \tag{A.12}$$

Band representations (BRs) are particular group representations that are induced by the irreducible represen-tation of the site-symmetry group at the Wyckoff positions. Elementary band representations (EBRs) are BRs thatcannot be further decomposed into multiples of BRs. These are induced by localized orbitals at maximal Wyckoff

A representation of a group over some vector space V is a collection of linear operators on this vector space, which satisfy the same algebra as the group elements. For finite groups, this operators can be simply matrices. Then, an irreducible representation is a set of matrix operators that are block-diagonalized simultaneously and cannot be divided into smaller parts.

B

WANNIER FUNCTIONS

Although the concept of Wannier functions (WF) dates back to 1937 [110], it has become an important computational tool in materials science. Especially, an intimate connection between the spatial localization of Wannier states and the properties of corresponding Bloch states provides insights into understanding of topological phases. Wannier functions also simplify computing polarization - instead of integrating over the Berry phase, it is enough to sum the Wannier charge centers **??**.

The main objective is to construct the real-space localized basis. As the Wannier functions span the same single-particle Hilbert space as the Bloch states, they share the same eigenvalue spectrum.

The Wannier function of an isolated band n is defined as

$$w_n(\mathbf{r}-\mathbf{R}) = \frac{V}{(2\pi)^d}\int_{BZ} d\mathbf{k} e^{-i\mathbf{k}\cdot\mathbf{R}}\psi_{n,\mathbf{k}}(\mathbf{k}). \tag{B.1}$$

Here, V correspond to the unit cell volume in d dimension and $\psi_{n,\mathbf{k}}(\mathbf{k})$ is the Bloch state for the n-th band. All the original Bloch states can all be exactly reproduced from a linear combination of the WF

$$\psi_{n,\mathbf{k}}(\mathbf{k}) = \sum_{\mathbf{R}} e^{i\mathbf{k}\cdot\mathbf{R}} w_n(\mathbf{r}-\mathbf{R}). \tag{B.2}$$

From Eq. (B.1), it is easily seen that Wannier functions are not uniquely defined. For instance, multiplying the Bloch state by $U(1)$ phase factor, $|\mathbf{k}, n\rangle \to e^{i\phi(\mathbf{k})}|\mathbf{k}, n\rangle$, which acts locally in reciprocal space, leaves the physical observables invariant. However, it changes the shape of basis functions in real space. WF center, $\langle w|\mathbf{r}|w\rangle$, is gauge-independent.

The generalization to a set of isolated bands is

$$w_(\mathbf{r}-\mathbf{R}) = \frac{V}{(2\pi)^d}\int_{BZ} d\mathbf{k} e^{-i\mathbf{k}\cdot\mathbf{R}}\psi_{n,\mathbf{k}}(\mathbf{k}).$$

(B.3)

In case of N occupied bands there is additional $U(N)$ gauge freedom:

$$\psi_{n,\mathbf{k}} \longrightarrow \sum_m U_{mn}(\mathbf{k})\psi_{m,\mathbf{k}}$$

The standard choice is to make a unitary transformation of the occupied bands only, thus resulting in as many WF as there are occupied bands.

only the sum over the Wannier centers in a given unit cell remains the same. Because of that gauge freedom, it

B.1 MAXIMALLY LOCALIZED WANNIER FUNCTIONS

One of the possible choice of a matrix U is to minimize the spread

$$\Omega = \sum_n \langle r^2\rangle_n - \langle \mathbf{r}\rangle_n^2 . \tag{B.5}$$

Ω can be spllitted into two parts, gauge invariant Ω_I and gauge dependent $\tilde{\Omega}$

$$\begin{aligned} \Omega &:= \Omega_I + \tilde{\Omega} \\ \Omega_I &= \sum_n \langle r^2 \rangle_n - \sum_{\mathbf{R},n,m} |\langle \mathbf{R}, m|\mathbf{r}|0, n\rangle|^2 \\ \tilde{\Omega} &\sum_n \sum_{\mathbf{R},m} |\langle \mathbf{Rm}|\mathbf{r}|\mathbf{0n}\rangle^2 \end{aligned} \tag{B.6}$$

B.2 SYMMETRY CONSTRAINS

B.3 RELATION BETWEEN WANNIER FUNCTIONS AND WILSON LOOPS

C

ENTANGLEMENT ENTROPY FROM A SINGLE-PARTICLE CORRELATION MATRIX

We start with the non-interacting Hamiltonian $H = -\sum_{ij} t_{ij} c_i^\dagger c_j$, which is the most general bilinear function of the fermionic operators preserving the number of excitations $n_i = c_i^\dagger c_i$. Let us define the one-particle correlation function

$$C_{ij} = \langle c_i^\dagger c_j \rangle = \langle \psi | c_i^\dagger c_j | \psi \rangle \,,$$

where $|\psi\rangle$ is an eigenstate of H (Slater determinant), not necessarily the ground state. By using Wick's theorem, we can express four-point (and higher-order) correlation function in terms of two-point correlation function.

Consider only subsystem A of a composite system - i, j indices are now restricted to the A part. We can express C_{ij} through density matrix of a canonical statistical ensemble ($\rho = \exp(-\beta H)/Z$, $\beta = 1$)

$$\langle c_i^\dagger c_j \rangle = Tr(\rho c_i^\dagger c_j) = C_{ij}$$

To easily calculate the trace, we transform our Hamiltonian H into the diagonal basis. So we rewrite our creation/annihilation operators $c_i^\dagger, c_j$ as new fermionic operators:

$$\begin{aligned} c_i &= \sum_k \phi_k(i) a_k \\ c_j^\dagger &= \sum_k \phi_k^*(j) a_k^\dagger \end{aligned} \tag{C.1}$$

$\phi_k(i) = \langle i|k \rangle$ are the eigenvectors in the site basis $|i\rangle$ with corresponding eigenvalues ϵ_k.

$$H = -\sum_{ij} t_{ij} c_i^\dagger c_j \xrightarrow{diag} H = \sum_k t_{ij} \phi_k^*(i) \phi_k(j) a_k^\dagger a_k = \sum_k \epsilon_k a_k^\dagger a_k \tag{C.2}$$

The density matrix becomes

$$\rho = \frac{1}{Z} e^{-\sum_k \epsilon_k a_k^\dagger a_k},$$

while the correlation function is (M - number of states)

$$\begin{aligned} C_{ij} &= \frac{Tr\left(e^{-\sum_k \epsilon_k a_k^\dagger a_k} c_i^\dagger c_j\right)}{Z} = \frac{Tr\left(\sum_k \phi_k(i) \phi_k^*(j) e^{-\epsilon_k a_k^\dagger a_k} a_k^\dagger a_k\right)}{Tr\left(\sum_k e^{-\epsilon_k a_k^\dagger a_k}\right)} \\ &= \frac{\sum_{k=1}^M \phi_k(i) \phi_k^*(j) \langle k| e^{-\epsilon_k a_k^\dagger a_k} a_k^\dagger a_k |k\rangle + \langle 0| e^0 a_0^\dagger a_0 |0\rangle}{\langle 0|e^0|0\rangle + \sum_{k=1}^M \langle k| e^{-\epsilon_k a_k^\dagger a_k} |k\rangle} \\ &= \sum_k \phi_k(i) \phi_k^*(j) \frac{(e^{-\epsilon_k} + 0)}{1 + e^{-\epsilon_k}} = \sum_k \phi_k(i) \phi_k^*(j) \frac{1}{(1 + e^{-\epsilon_k}) e^{\epsilon_k}} \\ &= \boxed{\sum_k \phi_k(i) \phi_k^*(j) \frac{1}{1 + e^{\epsilon_k}}} \end{aligned} \tag{C.3}$$

If we denote ζ_k as eigenvalues of C_{ij}, then the relation between ζ_k and ϵ_k is

$$\zeta_k = \frac{1}{1 + e^{\epsilon_k}} \tag{C.4}$$

C.1 SINGULAR VALUE DECOMPOSITION

Let M be a $m \times n$ matrix whose entries $\in \mathbb{C}$. Therefore, there exists a factorization of the form

$$M = U\Sigma V^{\dagger}$$

where U is a $m \times m$ unitary matrix ($U^{\dagger}U = \mathbb{1}$), Σ is a $m \times n$ diagonal matrix with non-negative elements, and $V^{\dagger}$ is a $n \times n$ unitary matrix. The vectors in the matrices U and V are orthonormal, so they represent rotations. Moreover, U and V are usually not related to each other at all. Σ_{ii} elements are all real and non-negative. The SVD always exist for any sort of rectangular or square matrix.

BIBLIOGRAPHY

1. Ginzburg, V. L. & Landau, L. D. On the Theory of superconductivity. *Zh. Eksp. Teor. Fiz.* **20**, 1064 (1950).
2. Berezinsky, V. L. Destruction of long range order in one-dimensional and two-dimensional systems having a continuous symmetry group. I. Classical systems. *Sov. Phys. JETP* **32**. [Zh. Eksp. Teor. Fiz.59,907(1971)], 493 (1971).
3. Berezinsky, V. L. Destruction of Long-range Order in One-dimensional and Two-dimensional Systems Possessing a Continuous Symmetry Group. II. Quantum Systems. *Sov. Phys. JETP* **34**. [Zh. Eksp. Teor. Fiz.61,no.3,1144(1972)], 610 (1972).
4. Kosterlitz, J. M. & Thouless, D. J. Long range order and metastability in two dimensional solids and superfluids. (Application of dislocation theory). *Journal of Physics C: Solid State Physics* **5**, L124 (1972).
5. Kosterlitz, J. M. & Thouless, D. J. Ordering, metastability and phase transitions in two-dimensional systems. *Journal of Physics C: Solid State Physics* **6**, 1181 (1973).
6. Klitzing, K. v., Dorda, G. & Pepper, M. New Method for High-Accuracy Determination of the Fine-Structure Constant Based on Quantized Hall Resistance. *Phys. Rev. Lett.* **45**, 494 (6 1980).
7. Tsui, D. C., Stormer, H. L. & Gossard, A. C. Two-Dimensional Magnetotransport in the Extreme Quantum Limit. *Phys. Rev. Lett.* **48**, 1559 (22 1982).
8. Mohr, P. J., Newell, D. B. & Taylor, B. N. CODATA Recommended Values of the Fundamental Physical Constants: 2014. *Journal of Physical and Chemical Reference Data* **45**, 043102 (2016).
9. Thouless, D. J., Kohmoto, M., Nightingale, M. P. & den Nijs, M. Quantized Hall Conductance in a Two-Dimensional Periodic Potential. *Phys. Rev. Lett.* **49**, 405 (6 1982).
10. Haldane, F. D. M. Model for a Quantum Hall Effect without Landau Levels: Condensed-Matter Realization of the "Parity Anomaly". *Phys. Rev. Lett.* **61**, 2015 (18 1988).
11. Read, N. & Green, D. Paired states of fermions in two dimensions with breaking of parity and time-reversal symmetries and the fractional quantum Hall effect. *Phys. Rev. B* **61**, 10267 (15 2000).
12. Wen, X. G. Vacuum degeneracy of chiral spin states in compactified space. *Phys. Rev. B* **40**, 7387 (10 1989).
13. Wen, X. G., Wilczek, F. & Zee, A. Chiral spin states and superconductivity. *Phys. Rev. B* **39**, 11413 (16 1989).
14. Wen, X.-G. Colloquium: Zoo of quantum-topological phases of matter. *Rev. Mod. Phys.* **89**, 041004 (4 2017).
15. Nayak, C., Simon, S. H., Stern, A., Freedman, M. & Das Sarma, S. Non-Abelian anyons and topological quantum computation. *Rev. Mod. Phys.* **80**, 1083 (3 2008).
16. Altland, A. & Zirnbauer, M. R. Nonstandard symmetry classes in mesoscopic normal-superconducting hybrid structures. *Phys. Rev. B* **55**, 1142 (2 1997).

17. Schnyder, A. P., Ryu, S., Furusaki, A. & Ludwig, A. W. W. Classification of topological insulators and superconductors in three spatial dimensions. *Phys. Rev. B* **78**, 195125 (19 2008).

18. Kitaev, A. Periodic table for topological insulators and superconductors. *AIP Conference Proceedings* **1134**, 22 (2009).

19. Ryu, S., Schnyder, A. P., Furusaki, A. & Ludwig, A. W. W. Topological insulators and superconductors: tenfold way and dimensional hierarchy. *New Journal of Physics* **12**, 065010 (2010).

20. Fu, L. & Kane, C. L. Topological insulators with inversion symmetry. *Phys. Rev. B* **76**, 045302 (4 2007).

21. Sheng, D. N., Weng, Z. Y., Sheng, L. & Haldane, F. D. M. Quantum Spin-Hall Effect and Topologically Invariant Chern Numbers. *Phys. Rev. Lett.* **97**, 036808 (3 2006).

22. Su, W. P., Schrieffer, J. R. & Heeger, A. J. Solitons in Polyacetylene. *Phys. Rev. Lett.* **42**, 1698 (25 1979).

23. Jotzu, G., Messer, M., Desbuquois, R., Lebrat, M., Uehlinger, T., Greif, D. & Esslinger, T. Experimental realization of the topological Haldane model with ultracold fermions. *Nature* **515**, 237 (2014).

24. Ding, Y., Peng, Y., Zhu, Y., Fan, X., Yang, J., Liang, B., Zhu, X., Wan, X. & Cheng, J. Experimental Demonstration of Acoustic Chern Insulators. *Phys. Rev. Lett.* **122**, 014302 (1 2019).

25. Kane, C. L. & Mele, E. J. Quantum Spin Hall Effect in Graphene. *Phys. Rev. Lett.* **95**, 226801 (22 2005).

26. Min, H., Hill, J. E., Sinitsyn, N. A., Sahu, B. R., Kleinman, L. & MacDonald, A. H. Intrinsic and Rashba spin-orbit interactions in graphene sheets. *Phys. Rev. B* **74**, 165310 (16 2006).

27. Yao, Y., Ye, F., Qi, X.-L., Zhang, S.-C. & Fang, Z. Spin-orbit gap of graphene: First-principles calculations. *Phys. Rev. B* **75**, 041401 (4 2007).

28. Hasan, M. Z. & Kane, C. L. Colloquium: Topological insulators. *Rev. Mod. Phys.* **82**, 3045 (4 2010).

29. Bernevig, B. A. & Zhang, S.-C. Quantum Spin Hall Effect. *Phys. Rev. Lett.* **96**, 106802 (10 2006).

30. Bernevig, B. A., Hughes, T. L. & Zhang, S.-C. Quantum Spin Hall Effect and Topological Phase Transition in HgTe Quantum Wells. *Science* **314**, 1757 (2006).

31. König, M., Wiedmann, S., Brüne, C., Roth, A., Buhmann, H., Molenkamp, L. W., Qi, X.-L. & Zhang, S.-C. Quantum Spin Hall Insulator State in HgTe Quantum Wells. *Science* **318**, 766 (2007).

32. Liu, C., Hughes, T. L., Qi, X.-L., Wang, K. & Zhang, S.-C. Quantum Spin Hall Effect in Inverted Type-II Semiconductors. *Phys. Rev. Lett.* **100**, 236601 (23 2008).

33. Knez, I., Du, R.-R. & Sullivan, G. Evidence for Helical Edge Modes in Inverted InAs/GaSb Quantum Wells. *Phys. Rev. Lett.* **107**, 136603 (13 2011).

34. Murakami, S. Quantum Spin Hall Effect and Enhanced Magnetic Response by Spin-Orbit Coupling. *Phys. Rev. Lett.* **97**, 236805 (23 2006).

35. Shechtman, D., Blech, I., Gratias, D. & Cahn, J. W. Metallic Phase with Long-Range Orientational Order and No Translational Symmetry. *Phys. Rev. Lett.* **53**, 1951 (20 1984).
36. Kraus, Y. E., Lahini, Y., Ringel, Z., Verbin, M. & Zilberberg, O. Topological States and Adiabatic Pumping in Quasicrystals. *Phys. Rev. Lett.* **109**, 106402 (10 2012).
37. Chen, R., Chen, C.-Z., Gao, J.-H., Zhou, B. & Xu, D.-H. Higher-Order Topological Insulators in Quasicrystals. *Phys. Rev. Lett.* **124**, 036803 (3 2020).
38. Varjas, D., Lau, A., Pöyhönen, K., Akhmerov, A. R., Pikulin, D. I. & Fulga, I. C. Topological Phases without Crystalline Counterparts. *Phys. Rev. Lett.* **123**, 196401 (19 2019).
39. Agarwala, A. & Shenoy, V. B. Topological Insulators in Amorphous Systems. *Phys. Rev. Lett.* **118**, 236402 (23 2017).
40. Fulga, I. C., van Heck, B., Edge, J. M. & Akhmerov, A. R. Statistical topological insulators. *Phys. Rev. B* **89**, 155424 (15 2014).
41. Mandelbrot, B., Freeman, W. & Company. *The Fractal Geometry of Nature* (Henry Holt and Company, 1983).
42. Gefen, Y., Mandelbrot, B. B. & Aharony, A. Critical Phenomena on Fractal Lattices. *Phys. Rev. Lett.* **45**, 855 (11 1980).
43. Carmona, J. M., Marconi, U. M. B., Ruiz-Lorenzo, J. J. & Tarancón, A. Critical properties of the Ising model on Sierpinski fractals: A finite-size scaling-analysis approach. *Phys. Rev. B* **58**, 14387 (21 1998).
44. Nakayama, T. & Yakubo, K. *Fractal concepts in condensed matter physics* (Springer Science & Business Media, 2013).
45. Van Veen, E., Yuan, S., Katsnelson, M. I., Polini, M. & Tomadin, A. Quantum transport in Sierpinski carpets. *Phys. Rev. B* **93**, 115428 (11 2016).
46. Van Veen, E., Tomadin, A., Polini, M., Katsnelson, M. I. & Yuan, S. Optical conductivity of a quantum electron gas in a Sierpinski carpet. *Phys. Rev. B* **96**, 235438 (23 2017).
47. Westerhout, T., van Veen, E., Katsnelson, M. I. & Yuan, S. Plasmon confinement in fractal quantum systems. *Phys. Rev. B* **97**, 205434 (20 2018).
48. Pal, B. & Chakrabarti, A. Staggered and extreme localization of electron states in fractal space. *Phys. Rev. B* **85**, 214203 (21 2012).
49. Pal, B., Patra, P., Saha, J. P. & Chakrabarti, A. Engineering wave localization in a fractal waveguide network. *Phys. Rev. A* **87**, 023814 (2 2013).
50. Kosior, A. & Sacha, K. Localization in random fractal lattices. *Phys. Rev. B* **95**, 104206 (10 2017).
51. Pal, B. & Chakrabarti, A. Nature of electron states and magneto-transport in a graphene geometry with a fractal distribution of holes. *Eur. Phys. J. B* **85**, 307 (2012).
52. Chen, T. L., Dikken, D. J., Prangsma, J. C., Segerink, F. & Herek, J. L. Characterization of Sierpinski carpet optical antenna at visible and near-infrared wavelengths. *New Journal of Physics* **16**, 093024 (2014).
53. Kempkes, S. N., Slot, M. R., Freeney, S. E., Zevenhuizen, S. J. M., Vanmaekelbergh, D., Swart, I. & Smith, C. M. Design and characterization of electrons in a fractal geometry. *Nature Physics* **15**, 127 (2019).

54. Shang, J., Wang, Y., Chen, M., Dai, J., Zhou, X., Kuttner, J., Hilt, G., Shao, X., Gottfried, J. M. & Wu, K. Assembling molecular Sierpinski triangle fractals. *Nature Chemistry* **7**, 389 (2015).
55. Ghez, J., Wang, Y. Y., Rammal, R., Pannetier, B. & Bellissard, J. Band spectrum for an electron on a Sierpinski gasket in a magnetic field. *Solid State Communications* **64**, 1291 (1987).
56. Alexander, S. Some properties of the spectrum of the Sierpinski gasket in a magnetic field. *Phys. Rev. B* **29**, 5504 (10 1984).
57. Rammal, R. & Toulouse, G. Spectrum of the Schrödinger Equation on a Self-Similar Structure. *Phys. Rev. Lett.* **49**, 1194 (16 1982).
58. Lindquist, B. & Riklund, R. Effects of deterministic aperiodic and self-similar on-site potentials on the structure of the Hofstadter butterfly. *Phys. Rev. B* **60**, 10054 (14 1999).
59. Agarwala, A., Pai, S. & Shenoy, V. B. Fractalized Metals. *ArXiv e-prints* (2018).
60. Pai, S. & Prem, A. Topological states on fractal lattices. *Phys. Rev. B* **100**, 155135 (15 2019).
61. Fremling, M., van Hooft, M., Smith, C. M. & Fritz, L. Existence of robust edge currents in Sierpiński fractals. *Phys. Rev. Research* **2**, 013044 (1 2020).
62. Iliasov, A. A., Katsnelson, M. I. & Yuan, S. Hall conductivity of a Sierpiński carpet. *Phys. Rev. B* **101**, 045413 (4 2020).
63. Hofstadter, D. R. Energy levels and wave functions of Bloch electrons in rational and irrational magnetic fields. *Phys. Rev. B* **14**, 2239 (6 1976).
64. Domany, E., Alexander, S., Bensimon, D. & Kadanoff, L. P. Solutions to the Schrödinger equation on some fractal lattices. *Phys. Rev. B* **28**, 3110 (6 1983).
65. Banavar, J. R., Kadanoff, L. & Pruisken, A. M. M. Energy spectrum for a fractal lattice in a magnetic field. *Phys. Rev. B* **31**, 1388 (3 1985).
66. Wang, X. R. Magnetic-field effects on localization in a fractal lattice. *Phys. Rev. B* **53**, 12035 (18 1996).
67. Kitaev, A. Anyons in an exactly solved model and beyond. *Annals of Physics* **321**. January Special Issue, 2 (2006).
68. Laughlin, R. B. Levitation of Extended-State Bands in a Strong Magnetic Field. *Phys. Rev. Lett.* **52**, 2304 (25 1984).
69. Onoda, M., Avishai, Y. & Nagaosa, N. Localization in a Quantum Spin Hall System. *Phys. Rev. Lett.* **98**, 076802 (7 2007).
70. Prodan, E., Hughes, T. L. & Bernevig, B. A. Entanglement Spectrum of a Disordered Topological Chern Insulator. *Phys. Rev. Lett.* **105**, 115501 (11 2010).
71. Prodan, E. Disordered topological insulators: a non-commutative geometry perspective. *Journal of Physics A: Mathematical and Theoretical* **44**, 113001 (2011).
72. Slager, R.-J., Mesaros, A., Juricic, V. & Zaanen, J. The space group classification of topological band-insulators. *Nature Physics* **9**, 98 (2013).
73. Shiozaki, K. & Sato, M. Topology of crystalline insulators and superconductors. *Phys. Rev. B* **90**, 165114 (16 2014).
74. Shiozaki, K., Sato, M. & Gomi, K. Topology of nonsymmorphic crystalline insulators and superconductors. *Phys. Rev. B* **93**, 195413 (19 2016).

75. Shiozaki, K., Sato, M. & Gomi, K. Topological crystalline materials: General formulation, module structure, and wallpaper groups. *Phys. Rev. B* **95**, 235425 (23 2017).

76. Dong, X.-Y. & Liu, C.-X. Classification of topological crystalline insulators based on representation theory. *Phys. Rev. B* **93**, 045429 (4 2016).

77. Fu, L. Topological Crystalline Insulators. *Phys. Rev. Lett.* **106**, 106802 (10 2011).

78. Hsieh, T. H., Lin, H., Liu, J., Duan, W., Bansil, A. & Fu, L. Topological crystalline insulators in the SnTe material class. *Nature Communications* **3**, 982 (2012).

79. Benalcazar, W. A., Bernevig, B. A. & Hughes, T. L. Quantized electric multipole insulators. *Science* **357**, 61 (2017).

80. Langbehn, J., Peng, Y., Trifunovic, L., von Oppen, F. & Brouwer, P. W. Reflection-Symmetric Second-Order Topological Insulators and Superconductors. *Phys. Rev. Lett.* **119**, 246401 (24 2017).

81. Schindler, F., Cook, A. M., Vergniory, M. G., Wang, Z., Parkin, S. S. P., Bernevig, B. A. & Neupert, T. Higher-order topological insulators. *Science Advances* **4** (2018).

82. Bradlyn, B., Elcoro, L., Cano, J., Vergniory, M. G., Wang, Z., Felser, C., Aroyo, M. I. & Bernevig, B. A. Topological quantum chemistry. *Nature* **547**, 298 (2017).

83. Liu, S., Vishwanath, A. & Khalaf, E. Shift Insulators: Rotation-Protected Two-Dimensional Topological Crystalline Insulators. *Phys. Rev. X* **9**, 031003 (3 2019).

84. Fang, C. & Fu, L. New classes of topological crystalline insulators having surface rotation anomaly. *Science Advances* **5** (2019).

85. Hsu, C.-H., Huang, Z.-Q., Crisostomo, C. P., Yao, L.-Z., Chuang, F.-C., Liu, Y.-T., Wang, B., Hsu, C.-H., Lee, C.-C., Lin, H. & Bansil, A. Two-dimensional Topological Crystalline Insulator Phase in Sb/Bi Planar Honeycomb with Tunable Dirac Gap. *Scientific Reports* **6**, 18993 (2016).

86. Jia, Y.-z., Ji, W.-x., Zhang, C.-w., Li, P., Zhang, S.-f., Wang, P.-j., Li, S.-s. & Yan, S.-s. Prediction of topological crystalline insulators and topological phase transitions in two-dimensional PbTe films. *Phys. Chem. Chem. Phys.* **19**, 29647 (43 2017).

87. Thouless, D. J. Wannier functions for magnetic sub-bands. *Journal of Physics C: Solid State Physics* **17**, L325 (1984).

88. Thonhauser, T. & Vanderbilt, D. Insulator/Chern-insulator transition in the Haldane model. *Phys. Rev. B* **74**, 235111 (23 2006).

89. Brouder, C., Panati, G., Calandra, M., Mourougane, C. & Marzari, N. Exponential Localization of Wannier Functions in Insulators. *Phys. Rev. Lett.* **98**, 046402 (4 2007).

90. Soluyanov, A. A. & Vanderbilt, D. Wannier representation of $\mathbb{Z}_2$ topological insulators. *Phys. Rev. B* **83**, 035108 (3 2011).

91. Po, H. C., Watanabe, H. & Vishwanath, A. Fragile Topology and Wannier Obstructions. *Phys. Rev. Lett.* **121**, 126402 (12 2018).

92. Po, H. C., Vishwanath, A. & Watanabe, H. Symmetry-based indicators of band topology in the 230 space groups. *Nature Communications* **8**, 50 (2017).

93. Ono, S., Yanase, Y. & Watanabe, H. Symmetry indicators for topological superconductors. *Phys. Rev. Research* **1**, 013012 (1 2019).

94. Alexandradinata, A., Dai, X. & Bernevig, B. A. Wilson-loop characterization of inversion-symmetric topological insulators. *Phys. Rev. B* **89**, 155114 (15 2014).

95. Benalcazar, W. A., Bernevig, B. A. & Hughes, T. L. Quantized electric multipole insulators. *Science* **357**, 61 (2017).

96. Sheng, X.-L., Chen, C., Liu, H., Chen, Z., Yu, Z.-M., Zhao, Y. X. & Yang, S. A. Two-Dimensional Second-Order Topological Insulator in Graphdiyne. *Phys. Rev. Lett.* **123**, 256402 (25 2019).

97. Lee, E., Kim, R., Ahn, J. & Yang, B.-J. Two-dimensional higher-order topology in monolayer graphdiyne. *npj Quantum Materials* **5**, 1 (2020).

98. Aroyo, M., Perez-Mato, J., Orobengoa, D., Tasci, E., De La Flor, G. & Kirov, A. Crystallography online: Bilbao crystallographic server. *Bulgarian Chemical Communications* **43**, 183 (2011).

99. Aroyo, M. I., Kirov, A., Capillas, C., Perez-Mato, J. M. & Wondratschek, H. Bilbao Crystallographic Server. II. Representations of crystallographic point groups and space groups. *Acta Crystallographica Section A* **62**, 115 (2006).

100. Vergniory, M. G., Elcoro, L., Wang, Z., Cano, J., Felser, C., Aroyo, M. I., Bernevig, B. A. & Bradlyn, B. Graph theory data for topological quantum chemistry. *Phys. Rev. E* **96**, 023310 (2 2017).

101. Bender, C. M. & Boettcher, S. Real Spectra in Non-Hermitian Hamiltonians Having *PT* Symmetry. *Phys. Rev. Lett.* **80**, 5243 (24 1998).

102. Herviou, L., Bardarson, J. H. & Regnault, N. Defining a bulk-edge correspondence for non-Hermitian Hamiltonians via singular-value decomposition. *Phys. Rev. A* **99**, 052118 (5 2019).

103. Bernard, D. & LeClair, A. A Classification of Non-Hermitian Random Matrices. *Statistical Field Theories*, 207 (2002).

104. Shen, H., Zhen, B. & Fu, L. Topological Band Theory for Non-Hermitian Hamiltonians. *Phys. Rev. Lett.* **120**, 146402 (14 2018).

105. Gong, Z., Ashida, Y., Kawabata, K., Takasan, K., Higashikawa, S. & Ueda, M. Topological Phases of Non-Hermitian Systems. *Phys. Rev. X* **8**, 031079 (3 2018).

106. Liu, C.-H., Jiang, H. & Chen, S. Topological classification of non-Hermitian systems with reflection symmetry. *Phys. Rev. B* **99**, 125103 (12 2019).

107. Yao, S. & Wang, Z. Edge States and Topological Invariants of Non-Hermitian Systems. *Phys. Rev. Lett.* **121**, 086803 (8 2018).

108. Song, F., Yao, S. & Wang, Z. Non-Hermitian skin effect and chiral damping in open quantum systems. *arXiv preprint arXiv:1904.08432* (2019).

109. Dresselhaus, M., Dresselhaus, G. & Jorio, A. *Group Theory: Application to the Physics of Condensed Matter* (Springer Berlin Heidelberg, 2007).

110. Wannier, G. H. The Structure of Electronic Excitation Levels in Insulating Crystals. *Phys. Rev.* **52**, 191 (3 1937).

CURRICULUM VITAE

PERSONAL DATA

Name	Marta Agnieszka Brzezińska
Date of Birth	August 22, 1991
Place of Birth	Legnica, Poland

EDUCATION

since 2015	Ph. D. in Physics, Faculty of Fundamental Problems of Technology, Wrocław University of Technology, Poland Supervisors: Prof. Titus Neupert, Prof. Arkadiusz Wójs
2013 – 2015	M. Sc. in Physics, Faculty of Fundamental Problems of Technology, Wrocław University of Technology, Poland Specialization: Physical Foundations of Computer Science Thesis: Entanglement entropy in d-dimensional interacting many-body systems Supervisor: Prof. Arkadiusz Wójs *Grade:* 5.5 (excellent)
2010 – 2013	B. Sc. in Physics, Faculty of Fundamental Problems of Technology, Wrocław University of Technology, Poland *Grade:* 5.0 (very good)

SCHOLARSHIPS & AWARDS

Nov 2019	Rector's Award for Best PhD Students in the academic year 2018/2019, Wrocław University of Science and Technology
Sep 2019 – Aug 2020	The Iwanowska Programme for Doctoral Students from Polish National Agency for Academic Exchange
Oct 2018 -– Sep 2019	Statutory Grant of the Wrocław University of Science and Technology for Young Researches
Sep 2018 – Aug 2019	Swiss Government Excellence Scholarship from Federal Commission for Scholarships for Foreign Students

PUBLICATIONS

Articles in peer-reviewed journals:

1. Schindler, F., Brzezińska, M., Benalcazar, W. A., Iraola, M., Bouhon, A., Tsirkin, S. S., Vergniory, M. G. & Neupert, T. Fractional corner charges in spin-orbit coupled crystals. *Phys. Rev. Research* **1**, 033074 (3 2019).
2. Guguchia, Z., Gawryluk, D. J., Brzezińska, M., Tsirkin, S. S., Khasanov, R., Pomjakushina, E., von Rohr, F. O., Verezhak, J. A. T., Hasan, M. Z., Neupert, T., Luetkens, H. & Amato, A. Nodeless superconductivity and its evolution with pressure in the layered dirac semimetal 2M-WS2. *npj Quantum Materials* **4**, 50 (2019).
3. Brzezińska, M., Cook, A. M. & Neupert, T. Topology in the Sierpiński-Hofstadter problem. *Phys. Rev. B* **98**, 205116 (20 2018).
4. Nouri, N., Bieniek, M., Brzezińska, M., Modarresi, M., Borujeni, S. Z., Rashedi, G., Wójs, A. & Potasz, P. Topological phases in Bi/Sb planar and buckled honeycomb monolayers. *Physics Letters A* **382**, 2952 (2018).
5. Brzezińska, M., Bieniek, M., Woźniak, T., Potasz, P. & Wójs, A. Entanglement entropy and entanglement spectrum of Bi_{1-x} Sb_x (111) bilayers. *Journal of Physics: Condensed Matter* **30**, 125501 (2018).
6. Radosz, W., Mielnik-Pyszczorski, A., Brzezińska, M. & Sznajd-Weron, K. *Q*-voter model with nonconformity in freely forming groups: Does the size distribution matter? *Phys. Rev. E* **95**, 062302 (6 2017).

Preprints (available on arXiv):

1. Hofmann, T., Helbig, T., Schindler, F., Salgo, N., Brzezińska, M., Greiter, M., Kiessling, T., Wolf, D., Vollhardt, A., Kabaši, A., Lee, C. H., Bilušić, A., Thomale, R. & Neupert, T. *Reciprocal skin effect and its realization in a topolectrical circuit* 2019.
2. Potasz, P., Jaworowski, B., Kupczyński, M., Brzezińska, M., Kaczmarkiewicz, P. & Wójs, A. *Topological phase transitions in Chern insulators within three-band models* 2017.